

# Venturing into Unexplored Phase Space: Synthesis, Structure, and Properties of $\text{MgCo}_3\text{B}_2$ Featuring a Rumped Kagomé Network

Paul Oftedahl, Nawsher J. Parvez, Zhen Zhang, Yang Sun, Vladimir Antropov, John Q. Xiao, and Julia V. Zaikina\*



Cite This: *Chem. Mater.* 2024, 36, 9834–9847



Read Online

ACCESS |

Metrics & More

Article Recommendations

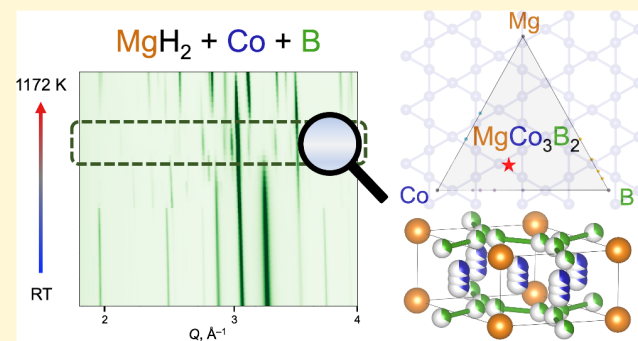
Supporting Information

**ABSTRACT:**  $\text{MgCo}_3\text{B}_2$ , a novel ternary boride in a previously unexplored phase space, was synthesized using the hydride route. In situ powder X-ray diffraction and DFT calculations aided in the discovery of this compound, whose structure was then determined by single-crystal X-ray diffraction. Like the closely related  $\text{CeCo}_3\text{B}_2$ ,  $\text{MgCo}_3\text{B}_2$  crystallizes in centrosymmetric space group  $P6/mmm$  ( $a = 4.883(2)$  Å,  $c = 2.926(2)$  Å at 210 K,  $Z = 1$ ). Unlike  $\text{CeCo}_3\text{B}_2$ , however, it adopts a disordered structure that features a rumped Kagomé network of Co atoms, and Mg atoms fill the channels of a Co–B framework. Although the structural disorder leads to motifs that are similar to those observed in  $\text{MgNi}_3\text{B}_2$  and other related ternary borides, no evidence of an ordered superstructure was found by single-crystal X-ray diffraction or high-resolution powder X-ray diffraction. In the case of  $\text{CeCo}_3\text{B}_2$ , boron atoms occupy the center of regular  $\text{Co}_6$  trigonal prisms; in  $\text{MgCo}_3\text{B}_2$ , boron atoms are shifted from the center of the prism to form B–B dimers with roughly the same length as those found in  $\text{MgNi}_3\text{B}_2$ . Magnetic susceptibility data exhibit an unusual temperature dependence that cannot be convincingly modeled by the modified Curie–Weiss equation, consistent with DFT calculations predicting a nonmagnetic ground state. Intrinsic susceptibility at 300 K is  $1.42 \times 10^{-3}$  emu/mol Oe, which is comparable to that of paramagnetic  $\text{YCo}_3\text{B}_2$  and  $\text{CeCo}_3\text{B}_2$  with a similar structure and composition. This study showcases the efficacy of combining several methodologies to discover new solids in unexplored phase spaces. This approach includes in situ PXRD data to monitor reactions of precursors upon heating, a diffusion-enhanced synthesis method, and DFT assessment of compound stability.

## INTRODUCTION

Borides are a class of materials whose diversity of structural motifs and compositional possibilities undergird a range of chemical and physical properties that make them relevant to a wide variety of technological applications.<sup>1–3</sup> Intermetallic borides and boron–metal alloys have long received attention for their outstanding physical properties such as ultrahardness and mechanical and thermal stability. Notable electrocatalytic and magnetic properties have been reported for binary and ternary intermetallic borides, including  $\text{MoB}_2$  as a catalyst for the hydrogen evolution reaction,<sup>4</sup>  $\text{Nd}_2\text{Fe}_{14}\text{B}$  displaying high magnetic coercivity,<sup>5</sup> and  $\text{AlFe}_2\text{B}_2$  exhibiting substantial magnetocaloric effect.<sup>6,7</sup> Boron-rich borides have been reported to exhibit superconductivity ( $\text{MgB}_2$ ,<sup>8</sup>  $\text{YB}_6$ )<sup>9</sup> and have the potential to exhibit significant thermoelectric effect owing to their complex crystal and electronic structures.<sup>2,10</sup>

Synthesis of borides is complicated by a number of factors: high temperatures are typically used owing to the inertness and high melting point of boron, but doing so tends to bypass metastable phases and can induce reactions with the container material.<sup>2,11</sup> This problem is compounded in the case of



ternary borides containing an alkali or alkaline-earth metal ( $A$ ) and a transition metal, where the differences in ductility, reactivity, and melting point between the  $A$  metals and boron work against the formation of the desired phases.<sup>12,13</sup> Of the systems  $A$ -T-B, compounds with  $T = \text{Ni}$  are known for  $A = \text{Li}$ ,  $\text{Mg}$ ,  $\text{Ca}$ ,  $\text{Sr}$ , and  $\text{Ba}$ , with  $\text{Mg}_3\text{Ni}_{20}\text{B}_6$  being the first example reported in 1963.<sup>14</sup> However, no ternary  $A$ -T-B borides with a first-row transition metal other than nickel have been published to date. Arc-melting elemental precursors in an inert atmosphere, a common approach to the synthesis of intermetallic borides in crystalline form, is not possible in these cases due to the high volatility of the  $A$  metal.<sup>1,13</sup>

Our key to expanding the compositional diversity of  $A$ -T-B compounds is the hydride route, where an alkali or alkaline-

Received: July 17, 2024

Revised: September 16, 2024

Accepted: September 17, 2024

Published: September 27, 2024



earth metal hydride is used in place of the metal itself. Substitution of a brittle, salt-like alkali or alkaline-earth metal hydride AH or AH<sub>2</sub> for a ductile metal permits precise compositional control and facilitates intimate mixing of precursors. This helps alleviate the kinetic hindrances inherent to solid-state reactions and enables rapid screening of new ternary systems by allowing reactions to proceed in less time and at lower temperatures.<sup>15,16</sup> The hydride route also facilitates the use of *in situ* monitoring of reactions via synchrotron powder X-ray diffraction, a technique that helps pinpoint the optimal synthesis temperature to produce a desired phase.<sup>17</sup> The search for new borides is further aided by DFT calculations of formation energy, electronic structure, and relevant properties such as magnetic ordering. Ultimately, *in situ* reaction monitoring and computational assessment of structure stability help eliminate the trial-and-error approach to the search for new solids.<sup>18</sup>

Recently, our group has confirmed computational predictions of new compounds in the Li–Ni–B system, and substitution studies have expanded to the quaternary Li–Ni–Co–B system.<sup>12,19–21</sup> However, despite theoretical predictions of stability and metastability, phases in the Li–Co–B ternary system have remained elusive.<sup>22</sup> Therefore, we decided to expand our efforts into the Mg–Co–B phase space, where no ternary compounds have hitherto been reported. An exploratory *in situ* powder X-ray diffraction experiment hinted at the formation of a ternary compound with a structure resembling MgNi<sub>3</sub>B<sub>2</sub>.<sup>23,24</sup> These findings were reinforced by DFT calculations indicating a low formation energy for the cobalt analog of MgNi<sub>3</sub>B<sub>2</sub>, which was further confirmed by *ex-situ* laboratory synthesis.

With respect to the potential properties of new ternary phases, switching from Ni to Co is advantageous due to the lower filling of the 3d band, increasing the likelihood of exchange interactions leading to long- or short-range magnetic order. Furthermore, the structure of MgNi<sub>3</sub>B<sub>2</sub> has a variety of features that prompt further exploration of the substitution of Ni for another first-row transition metal. MgNi<sub>3</sub>B<sub>2</sub> is a chiral intermetallic that crystallizes in space group P6<sub>4</sub>22; moreover, it features a slightly distorted, nonflat Kagomé network of Ni atoms, owing to the lack of mirror symmetry. The geometry of the Kagomé network, which consists of a 2D net of corner-sharing equilateral triangles, precludes the formation of an antiferromagnetic ground state with alternating up and down spins within a single layer, since not all pairs of spins can align in an antiparallel fashion. This could lead to magnetic frustration and related phenomena such as spin-glass or spin-ice states, superconductivity, charge-density waves, or potentially a quantum spin liquid state.<sup>25,26</sup> On the other hand, the distinctive symmetry of the network has implications for electronic structure, giving rise to phenomena such as massive and massless Dirac Fermions and flat bands.<sup>27–29</sup>

## ■ EXPERIMENTAL SECTION

**Synthesis of Polycrystalline MgCo<sub>3</sub>B<sub>2</sub> Powder.** MgCo<sub>3</sub>B<sub>2</sub> can be synthesized using both magnesium hydride and elemental magnesium Mg as the magnesium source. All precursors were manipulated in an argon-filled glovebox with an oxygen level below 1 ppm. For hydride synthesis, the following precursors were used: magnesium hydride (MgH<sub>2</sub>, Sigma-Aldrich, hydrogen storage grade), cobalt powder (Co, Alfa Aesar, 1.6 μm, 99.8% trace metals basis), boron powder (B, Sigma-Aldrich, crystalline, 60 mesh, 99% trace metals basis) in the experimentally optimized ratio MgH<sub>2</sub>:Co:B = 1.9:3:2.4 and total loading of 0.3 g. The powders were placed in

polystyrene grinding vials with slip-on caps and sealed inside two polypropylene bags in an argon atmosphere, then brought out of the glovebox. A SPEX Sample Prep 8000 M MIXER/MILL was used to ball-mill the powders for 18 min, after which the precursor mixture was placed in a niobium tube (roughly 1 cm diameter, 5 cm length) and sealed by arc-welding the end shut in an argon atmosphere.

For elemental synthesis, magnesium turnings (Mg, Alfa Aesar, 99.98%) washed with aqueous HCl were used in place of magnesium hydride along with the same cobalt and boron precursors in the experimentally optimized ratio Mg:Co:B = 2:3:2.4. Since Mg turnings cannot be easily ball-milled, only the Co and B powders were ball-milled (as described above). The Co/B precursor mixture was weighed before being placed in the bottom of a niobium tube, on top of which the magnesium turnings were placed. After weighing the Co/B mixture, the amount of magnesium was calculated to ensure a 2:3 ratio of magnesium to cobalt with a total typical mass of 0.3 g. At this point, the niobium tube was sealed under argon by arc-welding the end shut and was kept as vertical as possible until loading in the reactor.

For both synthesis routes, the sealed niobium tube was loaded into a silica reactor equipped with a Swagelok check valve to prevent the buildup of positive pressure in case of the release of hydrogen gas from the hydride reaction. The reactor was evacuated below  $3.5 \times 10^{-5}$  bar and placed into a resistance furnace (Thermo Scientific Thermolyne Type FD1500M) connected to a thermocontroller (Eurotherm 3216) and heated at 1.5 K/min to 1023 K, kept at that temperature for 48 h, and cooled by switching off the furnace. The byproduct of hydrogen gas embrittles the inside of the niobium tube but without compromising its structural integrity. To remove unreacted magnesium, the resulting powders were washed in dilute hydrochloric acid (pH between 1 and 2), rinsed with water and ethanol, and dried under vacuum.

**Synthesis of MgCo<sub>3</sub>B<sub>2</sub> Single Crystal.** In an attempt to obtain crystals of a suitable size for laboratory single-crystal X-ray diffraction (SC-XRD), the same synthesis procedure as described above for a precursor of elemental magnesium was used, with the following modifications: (1) an additional excess of magnesium was used, with the resulting ratio Mg:Co:B = 2.5:3:2.4, and (2) the following temperature profile was used: heating at 1.25 K/min to 1173 K, holding at that temperature for 48 h, cooling at 0.1 K/min to 1073 K, holding at that temperature for 100 h, cooling at 0.13 K/min to 673 K, and turning off the furnace. Due to the excess of magnesium, the resulting mass was firmly adhered to the bottom of the Nb tube, so the tube was opened at both ends and placed in mild HCl (pH ≈ 1) until the mass had broken free of the tube. A crystal suitable for SC-XRD was selected after rinsing samples with water and ethanol, drying in air, and gently crushing to break up large agglomerates.

**Laboratory Powder X-ray Diffraction.** Routine phase analysis of powdered samples was performed on powder diffractograms acquired using a Rigaku MiniFlex600 powder diffractometer with Cu K<sub>α</sub> radiation ( $\lambda = 1.54051 \text{ \AA}$ ) and a Ni K<sub>β</sub> filter. Zero-background plate holders composed of silica or a silicon single crystal were used to collect data at room temperature, and detector settings were chosen to minimize fluorescence of cobalt.

**High-Resolution Powder X-ray Diffraction.** High-resolution powder X-ray diffraction (HR-PXRD) measurements were acquired at the Low-Energy Wiggler beamline (WLE) of the Brockhouse Diffraction Sector at the Canadian Light Source at wavelength  $\lambda = 0.81931 \text{ \AA}$  at room temperature. A sample of MgCo<sub>3</sub>B<sub>2</sub> prepared from elemental magnesium was loaded in a silica capillary (0.5 mm inner diameter, 0.7 mm outer diameter) and sealed under vacuum. The capillary was mounted horizontally on a magnetic stub and spun during measurement at a rate of 2 Hz. Rietveld refinement of the powder diffractogram was carried out using the software GSAS-II.<sup>30</sup>

**Single-Crystal X-ray Diffraction.** A suitable crystal was isolated from a sample prepared as described above, from which diffraction data were collected up to  $2\theta = 90^\circ$  for a theoretical resolution of 0.50 Å. This was done in an effort to obtain high-angle reflections to aid in determining the absolute structure in case the crystal turned out to adopt a chiral structure, as is the case for MgNi<sub>3</sub>B<sub>2</sub>.<sup>24</sup> Data were

**Table 1. Structural Parameters of MgCo<sub>3</sub>B<sub>2</sub> as Refined from Single-Crystal XRD Data at 210 K<sup>a</sup>**

temperature		<i>a</i> (Å)	<i>c</i> (Å)	<i>V</i> (Å <sup>3</sup> )
210 K		4.883(2)	2.926(2)	60.42(6)
298 K		4.89245(2)	2.93110(1)	60.7594(3)
atom	Wyckoff site	<i>x/a</i>	<i>y/b</i>	<i>z/c</i>
Co1	3g	0.5	0	0.5
Co2	6i	0.5	0	0.382(1)
Mg1	1a	0	0	0
B1	6l	0.6106(6)	0.221(1)	0
				s.o.f. <i>U</i> <sub>eq</sub>
				1/3 0.0061(7) <sup>b</sup>

<sup>a</sup>Unit cell parameters from SCXRD and from high-resolution powder XRD at 298 K are compared. Anisotropic ADPs for Co and Mg atoms are given in Table S3. <sup>b</sup>*U*<sub>iso</sub> is used.

collected at 210 K on a Bruker D8 Venture diffractometer equipped with a Photon CMOS detector and cooled by an Oxford Cryosystem 800 low-temperature device, with a Mo K $\alpha$   $1\mu\text{s}$  radiation microsource giving a wavelength of 0.71073 Å.

Indexing by means of difference vectors in APEX3 software suggested a small hexagonal cell with  $a = b = 4.88$  Å,  $c = 2.93$  Å, equivalent to that adopted by CeCo<sub>3</sub>B<sub>2</sub> and other RC<sub>0.3</sub>B<sub>2</sub> compounds. After integrating and scaling SCXRD data in this small hexagonal cell to correct for absorption effects with SADABS,<sup>31</sup> XPREP software calculated a value of  $|E^2 - 1| = 0.964$ , remarkably close to the expected 0.968 of an ideal centric system. No systematic absences were found, so the lowest symmetry centrosymmetric space group  $P\bar{3}$  was chosen for an initial solution. The positions of the heavier atoms (Mg and Co) were determined using intrinsic phasing (SHELXT<sup>32</sup>). A combination of least-squares refinement and difference Fourier maps (SHELXL<sup>33</sup>) located substantial electron density ( $\sim 50$  e<sup>-</sup>) at around 0.4 Å from the Co 3f site, which was added as another Co atom in a 6g site and constrained such that the total occupancies of the 3f site and the two adjacent, symmetry-related instances of the 6g site sum to unity. B was found to be located in another 6g site, forming triangles with an unrealistically short B–B separation of 0.82 Å; the occupancy factor for the B site was constrained to 1/3 to avoid unrealistically short bond distances.

Further analysis of the atomic coordinates suggested that certain atomic sites are located close to what would be a special site in a space group of higher symmetry. Therefore, the structure was solved in supergroups of  $P\bar{3}$ . The coordinates (0.00010, 0.49987, *z*) of the Co2 site in the  $P\bar{3}$  space group are close to a 6i site (0, 1/2, *z*) in *P*6/*m*, a group where a mirror plane exists perpendicular to the *c*-axis. Refined coordinates of Co2 in these two solutions were not found to differ within the standard deviation (see Table S1). Additionally, the *z*-coordinate of the B site in  $P\bar{3}$  does not differ within standard deviation from 0, resulting in a 6j (*x*, *y*, 0) site in *P*6/*m*. Furthermore, the coordinates of the boron site were found to be very close to (*x*, 2*x*, 0), suggesting the group *P*6/*mmm* where these coordinates constitute a special 6l site, as a consequence of additional mirror planes containing the *c*-axis in *P*6/*mmm*. In all cases, the refined atomic coordinates and relative occupancies do not differ between solutions within standard deviations. The *P*6/*mmm* solution yielded the lowest *R* values while the goodness-of-fit increased slightly since this refinement was performed against fewer independent data owing to the higher symmetry. Therefore, the highest symmetry group *P*6/*mmm* was chosen (see Table S1 for a comparison of atomic coordinates and occupancies for solutions in all three groups).

In the final stages of refinement, anisotropic harmonic displacement parameters (ADP) were refined for Co and Mg, with Co1 and Co2 ADP constrained to be identical at all stages of the refinement. High-angle data ( $2\theta > 85^\circ$ ) were eliminated using the command OMIT –2 85 due to the low signal-to-noise ratio. A free refinement of the site occupancy of B site was attempted but resulted in occupancy of 34(1)%, which implies statistically possible cases of an unreasonably short B–B distance of 0.825 Å, although its ADP value remained reasonable. Therefore, for the final refinement, B site occupancy was fixed at 1/3. Cell parameters and atomic sites with occupancies and isotropic thermal parameters are listed in Table 1;

experimental parameters, crystallographic details, refinement statistics, and anisotropic thermal parameters are given in Tables S2 and S3. All crystal structures are plotted using the VESTA 3 visualization software.<sup>34</sup> Further details of the crystal structure refinement can be obtained from the Inorganic Crystal Structure Database (ICSD) from FIZ Karlsruhe–Leibniz Institute for Information Infrastructure ([www.fiz-karlsruhe.de](http://www.fiz-karlsruhe.de)) by quoting the CSD 2369299 deposition number at [www.ccdc.cam.ac.uk/structures](http://www.ccdc.cam.ac.uk/structures).

**Temperature-Resolved In Situ Powder X-ray Diffraction.** High-temperature in situ X-ray diffraction was used to investigate the formation mechanism and determine the synthesis temperature of MgCo<sub>3</sub>B<sub>2</sub>. To track in situ formation of MgCo<sub>3</sub>B<sub>2</sub>, data were collected at beamline 17-BM (Advanced Photon Source, Argonne National Laboratory) at wavelength  $\lambda = 0.24110$  Å between 298 and 1172 K, at a ramp rate of 20 K/min. The powders of magnesium hydride, cobalt, and boron taken in a 1:1:1 molar ratio were ball-milled for 18 min and sealed in a silica capillary (0.5 mm inner diameter, 0.7 mm outer diameter) under vacuum. The capillary was filled to approximately 1 cm with powder, and sealed with a length of at least 5 cm. In our experience, this provides adequate head space to prevent overpressurization and capillary explosion due to buildup of hydrogen gas from the hydride precursor. The sealed capillary was then mounted into a secondary shield capillary (0.9 mm inner diameter, 1.1 mm outer diameter) located on a sample stage equipped with two resistive microheaters and a thermocouple set as close to the measurement areas as possible.<sup>35</sup> The vertical setup was used for in situ data collection.<sup>36</sup> The uncertainty in the temperature measurement increases with temperature and is estimated to be  $\pm 30$  K above 873 K. Rietveld analysis was performed on selected patterns using GSAS-II.<sup>30</sup>

**Temperature-Resolved X-ray Diffraction of Prereacted MgCo<sub>3</sub>B<sub>2</sub>.** To study decomposition and thermal stability of MgCo<sub>3</sub>B<sub>2</sub>, a sample containing MgCo<sub>3</sub>B<sub>2</sub> as a major phase synthesized from elemental Mg was used. Data were collected at beamline 28-ID-2 (National Synchrotron Light Source II, Brookhaven National Lab) at wavelength  $\lambda = 0.1824$  Å between 298 and 1169 K. A capillary was filled with approximately 2.5 cm of powder and sealed with a length of 3 cm. The sample was mounted at the beamline in a horizontal setup and heated in a similar manner to the 17-BM measurement using a sample stage with two resistive heaters and a thermocouple.<sup>35</sup> The uncertainty in the temperature measurement increases with temperature and is estimated to be  $\pm 30$  K above 873 K.

**DFT Calculations.** Density functional theory (DFT) calculations were performed using VASP<sup>37</sup> employing the Perdew–Burke–Ernzerhof (PBE) generalized gradient approximation (GGA) exchange-correlation functional<sup>38</sup> and the projector augmented wave (PAW) method.<sup>39</sup> A plane-wave-basis set with a kinetic energy cutoff of 520 eV was used. The convergence thresholds were  $10^{-5}$  eV for electronic self-consistency and 0.01 eV Å<sup>-1</sup> for structural optimization. The Brillouin zone was sampled by the Monkhorst–Pack scheme<sup>40</sup> with a *k*-point grid of  $2\pi \times 0.033$  Å<sup>-1</sup> in the structural optimization and with a denser *k*-point grid of  $2\pi \times 0.022$  Å<sup>-1</sup> in the static calculation. The formation energies of MgCo<sub>3</sub>B<sub>2</sub> in the CeCo<sub>3</sub>B<sub>2</sub>, MgNi<sub>3</sub>B<sub>2</sub>, and ZrCo<sub>3</sub>B<sub>2</sub> structure types were obtained from spin-polarized calculations.

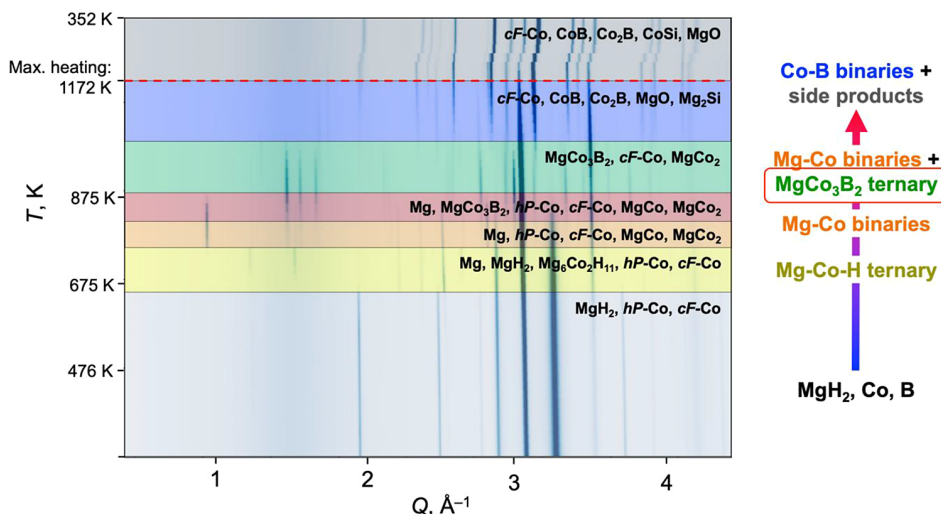


**Figure 1.** Temperature-resolved *in situ* powder X-ray diffraction of a precursor mixture containing powdered MgH<sub>2</sub>, Co, and B in a 1:1:1 ratio. Each horizontal section is a PXRD pattern where darker shading indicates higher relative intensity. The schematic on the right illustrates the proposed formation mechanism of MgCo<sub>3</sub>B<sub>2</sub>. Precursors MgH<sub>2</sub> and Co initially react to form a ternary hydride Mg<sub>6</sub>Co<sub>2</sub>H<sub>11</sub> and elemental Mg, which then react with excess Co to form two Mg–Co binary compounds. Next, the ternary boride MgCo<sub>3</sub>B<sub>2</sub> forms at 816 K and is stable up to 1016 K, where it transforms into Co–B binary compounds and products of side reactions with the silica capillary. The cobalt precursor consisted of hexagonal (*hP*-Co) and cubic (*cF*-Co) allotropes, and the hexagonal allotrope was observed to convert into the high-temperature stable face-centered cubic allotrope above 900 K. Data were collected at beamline 17-BM APS ANL at wavelength  $\lambda = 0.24110 \text{ \AA}$ .

**Differential Scanning Calorimetry.** DSC measurements were carried out using a Netzsch 404 F3 Pegasus Differential Scanning Calorimeter on a powdered sample sealed under vacuum in a silica ampule. Thermal stability was investigated by heating to 1173 K and cooling to 373 K, both at a rate of  $10\text{ K min}^{-1}$ .

**Magnetic Property Measurements.** Magnetization measurements were performed on a polycrystalline powder sample of  $\text{MgCo}_3\text{B}_2$  synthesized from magnesium hydride, sealed in a glass EPR tube under vacuum to prevent oxidation and sample loss. This sample was found to contain 83 wt %  $\text{MgCo}_3\text{B}_2$  from Rietveld refinement of laboratory PXRD with impurities of metallic Mg and antiperovskite  $\text{MgCo}_3(\text{B},\text{C})$ . A Quantum Design MPMS 3 SQUID magnetometer was used for measurements of *dc* magnetization as a function of temperature between 5 and 300 K at 0.1, 3.5, and 7 T fields, isothermal field-dependent magnetization up to 7 T at 5 and 300 K, and *ac* susceptibility (with 1 Oe *ac* field) at 1000 Oe *dc* bias field between 2 and 50 K and frequencies of 10, 100, and 1000 Hz.

## ■ RESULTS AND DISCUSSION

**In Situ Synthesis of MgCo<sub>3</sub>B<sub>2</sub>.** Unlike the systems A-Ni—B (A = Mg—Ba) where several ternary compounds have been reported with a variety of compositions and structures, no ternary compounds have yet been reported for Co-containing systems, including the Mg—Co—B system. To quickly screen for a novel ternary phases, an *in situ* synchrotron X-ray powder diffraction experiment was performed using a 1:1:1 molar ratio of MgH<sub>2</sub>, Co, and B powders. In an *in situ* synthesis reaction, powder X-ray diffraction (PXRD) patterns are collected incrementally during heating (and cooling) of unreacted precursors sealed in a silica capillary to reveal hidden phase transformations. The PXRD data from the *in situ* experiment are depicted as a waterfall plot in Figure 1, a stack of PXRD patterns where a darker shading corresponds to higher relative diffraction intensity. The patterns are arranged from bottom to top, so moving up the y-axis represents slow heating followed by fast cooling. A waterfall plot is a convenient way to show all the PXRD data from an *in situ* experiment in one graphic, and effectively conveys qualitative information about phase trans-

formations and identities. However, due to the conversion of peak intensity into gradations in shading in the waterfall plot, small peaks are not always discernible in such a representation, especially if they are found in a region with many other peaks nearby, so minor phases are easily overlooked. Therefore, it is essential to carefully inspect each PXRD pattern in succession and perform a Rietveld refinement whenever peaks appear or disappear. The phase fractions determined by such a set of refinements for this *in situ* data set are listed in [Table S4](#). Phase analysis on representative PXRD patterns from each region indicated in [Figure 1](#) is shown in [Figure S1](#). While most of the PXRD patterns for the Mg–Co–B experiment consisted of peaks that could be matched to known elements or binary phases, two regions (colored yellow and green in [Figure 1](#)) were found to be of particular interest; representative PXRD patterns from these regions are analyzed in [Figure 2](#).

The first transformation that takes place is the decomposition of  $\text{MgH}_2$  to elemental Mg, accompanied by the formation of the known ternary hydride  $\text{Mg}_6\text{Co}_2\text{H}_{11}$ . Early reports of this phase differ as to its exact composition and symmetry; a neutron diffraction study of the deuterated compound established the composition above and an orthorhombic structure in space group  $Pnma$ .<sup>41</sup> The initial reports describe heating under  $\sim 5$  MPa of hydrogen to produce this phase.<sup>41,42</sup> In the synthesis utilized here, decomposition of the  $\text{MgH}_2$  precursor in the sealed tube would have afforded the hydrogen pressures needed to form the phase. This ternary hydride appears to be stable over a relatively narrow temperature range of 696–756 K, above which it gives way to two different Mg–Co binary compounds:  $\text{MgCo}$ <sup>43</sup> and  $\text{MgCo}_2$ .<sup>44</sup> Peaks for the ternary hydride phase are indicated with gray boxes in Figure 2a.

Between 816 and 1016 K, a set of peaks is observed that cannot be matched to known phases composed of Mg, Co, B, and H. The locations and intensities of these peaks resemble those of  $\text{MgNi}_3\text{B}_2$ , as shown in Figure 2b. Although some of these peaks overlap with or are nearby those of  $\text{MgCo}_2$ , a

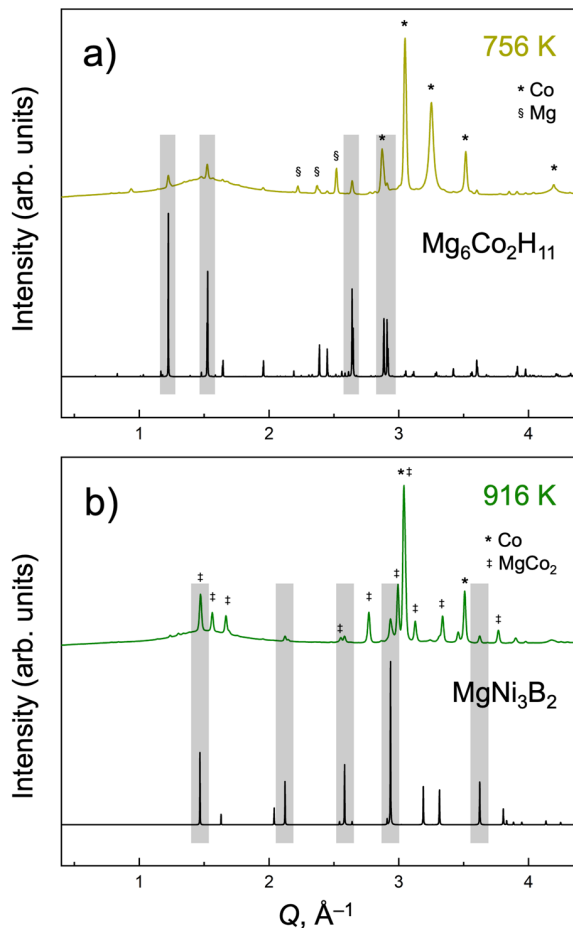


**Figure 2.** Selected PXRD patterns from an in situ reaction of  $MgH_2$ , Co, and B. Top patterns are measured data at the temperature indicated; bottom patterns are theoretical patterns for the specified phase. The gray boxes highlight the major peaks of the phases of interest and serve as a guide to the eye. (a) in PXRD pattern at 756 K, small peaks corresponding to the  $Mg_6Co_2H_{11}$  phase are highlighted; (b) PXRD pattern at 916 K contains small peaks that do not match any known phases composed of Mg, Co, B, and/or H but are quite close to predicted peaks for  $MgNi_3B_2$ . Both patterns feature large peaks for major phases as indicated with symbols, and other small peaks for minor impurity phases. For a more thorough phase analysis of these and other representative patterns, see Figure S1.

major phase at this temperature, Rietveld analysis clearly indicated unaccounted peak intensity at the locations indicated by gray boxes in Figure 2b. This prompted DFT evaluation of the phase with composition  $MgCo_3B_2$  in the  $MgNi_3B_2$  structure, which revealed a favorable formation energy of  $-37.7467$  eV/f.u. for this potential compound. Interestingly,  $MgCo_3B_2$  is not identified as a stable compound in available databases of high-throughput materials predictions.<sup>45–48</sup> In the in situ experiment, the ternary boride persists up to 1016 K, although its weight fraction never exceeds 12.4 wt %, derived from Rietveld analysis of the PXRD pattern measured at 916 K. Both  $MgCo_3B_2$  and  $MgCo_2$  cease to be observed above 1016 K, a range in which Co–B binary compounds prevail, as well as  $Mg_2Si$ ,  $CoSi$ , and  $MgO$  formed by side reactions with the silica capillary walls.

In summary, the in situ synthesis experiment strongly suggests the existence of a new ternary boride phase with composition  $MgCo_3B_2$ , in analogy to the known phase

$MgNi_3B_2$ . Peaks for this compound are only observed in the range 816–1016 K, suggesting that this phase becomes less energetically favorable with respect to Co–B binary compounds at  $T > 1000$  K and providing insight into the temperature range suitable for ex situ synthesis. The observed set of reactions comprising the formation and decomposition of this phase is quite complex:  $MgH_2$  and Co react to form the ternary hydride phase  $Mg_6Co_2H_{11}$ , then excess Co reacts with this phase or Mg from the decomposition of  $MgH_2$  to form  $MgCo$  and  $MgCo_2$  binary phases. Above 816 K, the first boride is observed in the form of ternary  $MgCo_3B_2$ , which may be the product of the reaction of  $MgCo$  with excess Co and B, or of the three constituent elements individually. Above 1016 K, this compound reacts with the capillary walls to form  $MgO$  and  $Mg_2Si$ , leaving behind CoB and  $Co_2B$ . Complete elucidation of these structural transformations was only possible after careful Rietveld analysis of successive PXRD patterns accompanied by manual searching of several crystal structure databases.<sup>49–51</sup> Attempts to automate this process are highly prone to error and often lead to misidentification of major phases while minor components are overlooked entirely.<sup>52</sup>

**Ex Situ Synthesis of  $MgCo_3B_2$ .** Guided by insight from the in situ diffraction experiment, ex situ synthesis of  $MgCo_3B_2$  was initially carried out using magnesium hydride and elemental cobalt and boron precursors. A loading composition of  $MgH_2:Co:B = 1.8:3:2.4$  was chosen in analogy to the optimized composition of  $LiH:Ni:B = 1.7:3:2.4$  used for  $LiNi_3B_{1.8}$ , a closely related phase (vide infra) that has been successfully synthesized using the hydride route.<sup>13</sup> In our experience, an excess of alkali/alkaline-earth element is often found to be necessary to stabilize a given phase; in some cases, the excess may exceed 2-fold. Unlike  $LiNi_3B_{1.8}$ , however, which forms in the highest purity after a short dwell at 1173 K followed by a longer dwell at 1023 K, in situ diffraction suggests that  $MgCo_3B_2$  is a less favored phase at temperatures above 1023 K. This was confirmed by initial attempts at ex-situ synthesis, where an optimal synthesis temperature of 1023 K was determined. During the synthesis optimization, binary  $MgCo_2$  was frequently produced as a competing phase, particularly when decreasing the initial amount of magnesium and when starting from elemental magnesium. This aligns with in situ evidence, which shows peaks for  $MgCo_2$  across the entire range over which  $MgCo_3B_2$  is observed to be stable. In general, while  $MgCo_3B_2$  is observed to be formed from reactions spanning a wide range of compositional phase space and heating profiles, Mg–Co and Co–B binaries tend to prevail when the Mg:Co ratio is decreased below 1.8:3, and  $Co_2B$  is observed to form more readily above 1023 K.

To eliminate the possibility that this new compound might be a hydride-stabilized phase, attempts were made to synthesize it from elemental magnesium rather than magnesium hydride. This proved to be successful, although about 5% excess of magnesium was required when compared to the loading composition optimized for reaction from magnesium hydride. One of the advantages of the hydride route is that it permits precise control of precursor stoichiometry. Working from an elemental magnesium precursor meant that turnings of magnesium metal had to be added to ball-milled cobalt and boron, and the actual Mg:Co ratio usually deviated from the desired 2:3 by up to 0.05 with respect to 3 equivalents of cobalt. While this may not seem significant, it was found that decreasing the Mg:Co ratio even to 1.9:3, a difference of 0.1 relative to 3 equivalents of cobalt,

resulted in the formation of  $\text{MgCo}_3\text{B}_2$  as the major phase with little evidence of the ternary phase.

Growing crystals of  $\text{MgCo}_3\text{B}_2$  suitable for single-crystal X-ray diffraction proved to be challenging. Initial attempts involved the same preparation as described above for the synthesis of polycrystalline  $\text{MgCo}_3\text{B}_2$  from elemental magnesium with an extended dwell at 1073 K and slow cooling to 673 K. Then, a magnesium flux (3 equiv with respect to  $\text{MgCo}_3\text{B}_2$ ), as well as  $\text{MgCl}_2/\text{NaCl}$  eutectic and  $\text{MgCl}_2$  salt fluxes, were attempted. Each of these attempts resulted in crystal sizes too small for single-crystal X-ray diffraction in a laboratory setup. It was only when eliminating the flux and including an initial heating step at 1173 K for 48 h, a slow cool to 1073 K, and an extended dwell at that temperature for 100 h before the slow cooling step that the crystals of larger size began to form. However, even this optimized profile yielded only very small crystals ( $\approx 10 \mu\text{m}$  across) of irregular shape, most of which were comprised of multiple crystalline domains. A suitable crystal of dimensions  $5 \times 5 \times 15 \mu\text{m}$  was eventually isolated and used for data collection. Interestingly, Manfrinetti et al. in their report on  $\text{MgNi}_3\text{B}_2$  do not utilize a flux for crystal growth but found that extended dwelling at 1173 or 1223 K gave a sample from which a crystal (measuring  $40 \times 40 \times 110 \mu\text{m}$ ) could be isolated.<sup>24</sup>

**MgCo<sub>3</sub>B<sub>2</sub> Crystal Structure Solution.** From the initial indications of a new Mg–Co–B phase from in situ PXRD, it was apparent that the structure of this phase is closely related to that of  $\text{MgNi}_3\text{B}_2$ , whose structure and relation to other structure types have been previously discussed at length. In summary, the  $\text{MgNi}_3\text{B}_2$  structure type is a variant of the  $\text{CeCo}_3\text{B}_2$  structure type ( $P6/mmm$ ), which itself is a ternary ordered variant of  $\text{CaCu}_5$ .<sup>24</sup> In the  $\text{CeCo}_3\text{B}_2$  structure, B is six-coordinate by Co, forming  $\text{BCo}_6$  trigonal prisms that share edges along the  $c$ -direction and create hexagonal cavities filled by chains of Ce atoms along the  $c$ -direction. Ce and B atoms lie within the plane  $z = 0$ , while Co atoms occupy  $3c$  sites and form a perfect Kagomé network in the  $z = 1/2$  plane as dictated by the mirror symmetry.<sup>53</sup> In  $\text{MgNi}_3\text{B}_2$  ( $P6_{4}22$ ), mirror symmetry perpendicular to  $c$  is removed, which allows for a slight distortion of the Kagomé network of Ni atoms, and the 6-fold proper rotation axis is replaced by a screw axis, which allows B atoms to be slightly displaced from their special site ( $1/3, 2/3, 0$ ) to form dimers (B–B distance =  $1.876 \text{ \AA}$ ). The presence of this  $6_4$  screw axis also creates a 3-fold expansion of the unit cell along  $c$ , which in turn gives rise to additional reflections with indices  $l \neq 3n$ . Another variant of this structure is found in the case of  $\text{ZrCo}_3\text{B}_2$ , which adopts a rhombohedral cell ( $R\bar{3}$ ) and also features a ruffled Kagomé network of Co atoms as well as B dimers.<sup>54</sup> However, since the group  $R\bar{3}$  is not chiral, its symmetry dictates that the B dimers in adjacent layers be related by both  $3_1$  and  $3_2$  screw axes, while in the  $P6_{4}22$  structure, only a  $3_1$  axis is present. Additionally, a monoclinic variant of the  $\text{CeCo}_3\text{B}_2$  structure type has been reported for many  $RT_3\text{B}_2$  compounds, where  $T$  is a  $4d$  or  $5d$  element. This structure has the prototypical formula  $\text{ErIr}_3\text{B}_2$  and is only very slightly distorted from the  $\text{CeCo}_3\text{B}_2$  type; the cell is nearly orthorhombic with  $\beta \approx 90^\circ$ . The relationship between the unit cells of these structures are discussed in more detail in the Supporting Information; representative structures are plotted in projection onto the  $ab$ -plane in Figure 3.

Refinement of single-crystal XRD data was carried out in a hexagonal cell with  $a = b = 4.883 \text{ \AA}$ ,  $c = 2.926 \text{ \AA}$ , equivalent to the  $\text{CeCo}_3\text{B}_2$  cell. Further analysis (see Experimental) strongly

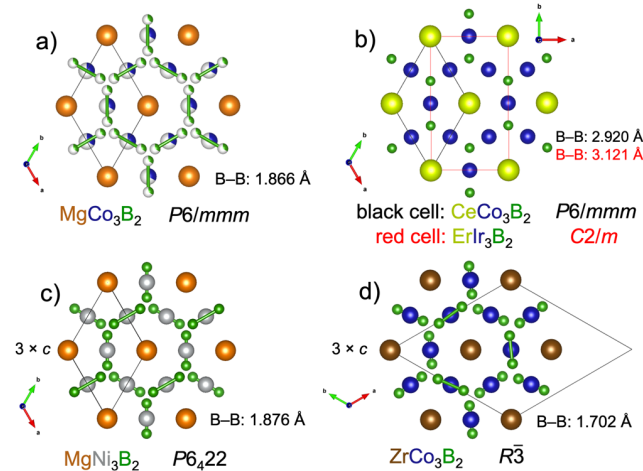


**Figure 3.** Projections along  $c$  of four different structure types derived from  $\text{CeCo}_3\text{B}_2$ : (a)  $\text{MgCo}_3\text{B}_2$  (this work), disordered variant of  $\text{CeCo}_3\text{B}_2$ ; (b)  $\text{CeCo}_3\text{B}_2$  and  $\text{ErIr}_3\text{B}_2$  featuring isolated boron atoms rather than dimers; (c)  $\text{MgNi}_3\text{B}_2$ , chiral variant of  $\text{CeCo}_3\text{B}_2$  featuring a  $6_4$  screw axis and  $3 \times c$  unit cell; and (d) rhombohedral  $\text{ZrCo}_3\text{B}_2$  in centrosymmetric space group  $R\bar{3}$  with conventional hexagonal setting. For relations between the cells plotted here, please refer to the Supporting Information.

suggested a centrosymmetric space group. After attempts in  $P\bar{3}$ ,  $P6/m$ , and  $P6/mmm$ , the highest symmetry  $P6/mmm$  was chosen. Structure solution using intrinsic phasing (SHELXT) located Mg and Co atoms in the same sites as Ce and Co in  $\text{CeCo}_3\text{B}_2$ . During least-squares refinement coupled with difference Fourier maps, significant electron density at around  $0.4 \text{ \AA}$  from Co was refined as a Co split site; B atoms were found to occupy a 6-fold site with occupancy factor constrained to  $1/3$ . The final refinement with anisotropic atomic displacement parameters (ADPs) for Mg and Co converged to  $R_1$  (all data) = 0.0248,  $wR_2$  = 0.0449, and  $\text{GoF} = 1.117$ . Details on the process of refining the crystal structure are provided in the Experimental section; unit cell parameters, atomic coordinates, site occupancy factors, and atomic displacement parameters are given in Table 1. Anisotropic thermal parameters and additional refinement details can be found in Tables S1–S3.

**MgCo<sub>3</sub>B<sub>2</sub> Crystal Structure Description.** The refined structural model with disordered Co and B sites as well as an average structure are shown in Figure 4a. In the average structure, which is equivalent to the ordered  $\text{CeCo}_3\text{B}_2$  structure, Co atoms occupy a 3-fold site ( $3g$ ) and B atoms occupy a 2-fold site ( $2c$ ). In  $\text{MgCo}_3\text{B}_2$ , what would be one Co atom in the  $\text{CeCo}_3\text{B}_2$  structure is split along the  $z$ -axis into three positions, each with roughly  $1/3$  occupancy: one  $\text{Co1}$  atom, located in a  $3g$  site with  $z$ -coordinate  $0.5c$ , and two  $\text{Co2}$  atoms, located in a  $6i$  site with  $z$ -coordinate  $(0.5 \pm 0.118)c$ . The separation between Co atoms at these two sites is  $0.118c$  or  $0.345 \text{ \AA}$ , so only one of the three positions can be occupied at a time. Likewise, what would be one B atom in the  $\text{CeCo}_3\text{B}_2$  structure at a  $2c$  site is shifted by  $0.475 \text{ \AA}$  within the plane  $z = 0$  into a  $6l$  site. The higher multiplicity of this site would lead to the formation of triangles of B atoms separated by  $0.822 \text{ \AA}$ , so the occupancy of this site was constrained to  $1/3$ , which makes such an unreasonable short B–B contact statistically impossible.

**B–B Interatomic Separations and Environment.** In the  $\text{CeCo}_3\text{B}_2$ -like ordered structure of  $\text{MgCo}_3\text{B}_2$ , Co atoms form

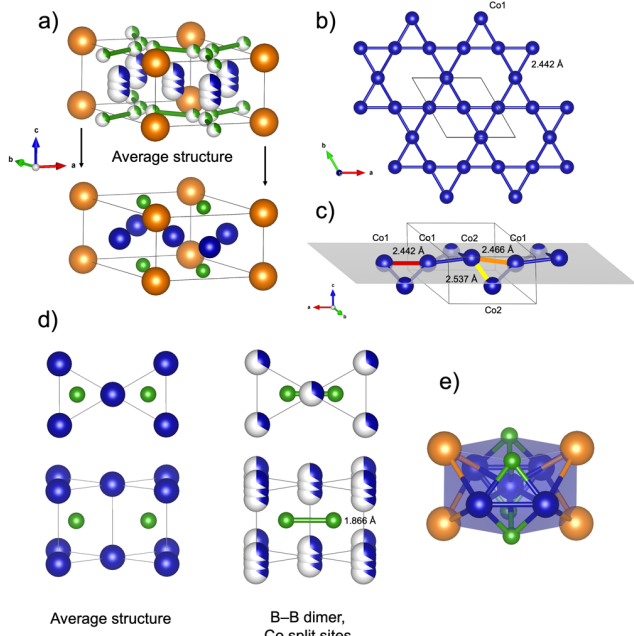


**Figure 4.** Structure of  $\text{MgCo}_3\text{B}_2$ . (a) Comparison of the disordered model of  $\text{MgCo}_3\text{B}_2$  with split Co and B sites and the average structure obtained by eliminating Co2 and moving B from a split 6l site to a fully occupied 2c site; (b) the idealized Kagomé network of only Co1 atoms viewed along the *c* axis; (c) a more realistic scenario in which interactions between neighboring Co atoms with differing *c*-coordinate are considered, with each of the three distinct bond distances outlined in a different color; (d) comparison of B–B interatomic separations and  $\text{BCo}_6$  coordination polyhedra between the average structure and the disordered structure with Co and B split sites and B–B dimers; and (e) capped rhombic prismatic geometry of 12-coordinate Co in the average structure.

trigonal prisms that share edges along the *c*-axis. Isolated B atoms lie in the center of these prisms, and the prisms themselves connect to form hexagonal channels running along the *c*-axis that would contain Mg atoms. In the disordered structure, partial occupancy of the Co split sites causes the  $\text{BCo}_6$  prisms to become distorted compared to the idealized geometry manifested in  $\text{CeCo}_3\text{B}_2$ . Additionally, the B atoms are displaced from the center of the prisms at  $(\frac{1}{3}, \frac{2}{3}, 0)$  to bond through the shared edge of two adjacent prisms and form a B–B dimer (Figure 4d) with a separation of 1.870 Å. This is remarkably close to the B–B distance in  $\text{MgNi}_3\text{B}_2$  of 1.876 Å, but longer than the B–B separation of 1.702 Å in  $\text{ZrCo}_3\text{B}_2$ . Importantly, this motif is part of what distinguishes the structures of  $\text{MgNi}_3\text{B}_2$  and  $\text{ZrCo}_3\text{B}_2$  from the higher-symmetry  $\text{CeCo}_3\text{B}_2$  structure adopted by all of the  $\text{RCO}_3\text{B}_2$  compounds.<sup>13</sup>

**Co–Co Kagomé Network.** In the  $\text{CeCo}_3\text{B}_2$  structure type, the substructure of Co atoms forms a perfect flat Kagomé network (Figure 4b). In  $\text{MgCo}_3\text{B}_2$ , the random distribution of Co across two split sites leads to a rumpling of the Kagomé network above and below the plane at *z* = 0.5*c*. In the case of  $\text{MgCo}_3\text{B}_2$ , for an idealized Kagomé network consisting only of fully occupied Co1 atoms, the distance between adjacent Co atoms would be 2.442 Å in all cases (Figure 4b). In the refined disordered model, three Co–Co bond distances are possible (Figure 4c). The first bond distance of 2.442 Å (shown in red in Figure 4c) occurs in the case of two adjacent Co atoms with the same *z*-coordinate, i.e., either between adjacent Co1 or adjacent Co2 atoms. The second bond distance is the one

found between a Co1 atom and a neighboring Co2 atom; these atoms will necessarily differ in their *z*-coordinate by 0.118*c*, leading to a greater separation of 2.466 Å (shown in orange in Figure 4c). Finally, a Co2 atom sitting above the plane *z* = 0.5*c* (shown in Figure 4c) may be connected to a Co2 atom sitting below this plane; in this case the *z*-coordinates of these two atoms differ by 0.236*c*, and the resulting separation is the longest at 2.537 Å (shown in yellow in Figure 4c). Each of these possible distances is reasonable for a Co–Co metallic bond: the Co–Co separation in metallic Co is 2.513 Å in the case of the cubic allotrope and 2.503 Å in the case of the hexagonal allotrope, while in  $\text{Co}_2\text{B}$  an even closer separation of 2.426 Å is observed. For in-depth discussion of coordination environments of Co and B, please refer to Figures S2 and S3 and the associated discussion.

To determine whether the observed disorder in the small cell is a superposition of multiple Co sites exhibiting long-range order (creating a supercell or incommensurately modulated structure) or short-range order (resulting in diffuse scattering), precession images of reconstructed reciprocal lattice planes were analyzed (Figure S4). Although a number of faint streaks and spots were observed in reciprocal planes *h*0*l*, 0*k**l*, and *h**h**l*, they do not form any regular patterns that would be suggestive of a superstructure or of higher-dimensional symmetry, nor are the observed reflections elongated in any direction, which would be indicative of diffuse scattering. These images provide compelling evidence that the primitive hexagonal cell chosen for single-crystal refinement is best suited for the  $\text{MgCo}_3\text{B}_2$  structure. The case of  $\text{Mg}_2\text{Rh}_{1-x}\text{B}_{6+2x}$  is in some ways akin to the structure in question: both  $\text{MgCo}_3\text{B}_2$  and  $\text{Mg}_2\text{Rh}_{1-x}\text{B}_{6+2x}$  are disordered variants of an ordered *R*–T–B compound (*viz.*,  $\text{CeCo}_3\text{B}_2$  and  $\text{Y}_2\text{ReB}_6$ ) where site splitting is observed without indications of a superstructure. In the case of  $\text{Mg}_2\text{Rh}_{1-x}\text{B}_{6+2x}$ , the disordered structure in a primitive orthorhombic cell features a position split between Rh and a B dimer, and electron diffraction images were used to rule out the possibility of a superstructure.<sup>55</sup>

**Rietveld Analysis of HR-PXRD for  $\text{MgCo}_3\text{B}_2$ .** To help confirm the validity of the structural model refined from single-crystal X-ray diffraction, a Rietveld refinement was attempted using high-resolution PXRD data. The result was compared to that of similar refinements using structural models for  $\text{MgNi}_3\text{B}_2$ ,  $\text{ZrCo}_3\text{B}_2$ , and  $\text{CeCo}_3\text{B}_2$  with appropriate atomic substitutions and unit cell parameter adjustments (Figures S5–S7, Tables S5 and S6). For these refinements, known impurity phases were added, and all unit cell parameters, background coefficients, scale factor, and phase fractions were refined. Because the models for  $\text{MgNi}_3\text{B}_2$  and  $\text{ZrCo}_3\text{B}_2$  feature a superstructure, additional peaks are predicted that are lacking in the experimental pattern (marked in Figures S5 and S6). The structure for  $\text{CeCo}_3\text{B}_2$  adopts the same unit cell as the model for  $\text{MgCo}_3\text{B}_2$  refined from SCXRD data with no additional diffraction peaks. However, the  $\text{CeCo}_3\text{B}_2$  model does not accurately describe the observed peak intensities since there are multiple peaks with a significant disparity in intensity between the  $\text{CeCo}_3\text{B}_2$  model and the observed pattern (marked in Figure S7). Only the disordered  $\text{CeCo}_3\text{B}_2$ -like structure obtained from SCXRD can correctly fit the powder diffraction data; alternate, ordered models either do not correctly model observed peak intensities or give rise to extraneous peaks as a result of a superstructure.

After refining several sample parameters, including phase fractions of impurity phases, Rietveld refinement of the SCXRD model yielded a  $wR$  value of 0.038 with  $\text{MgCo}_3\text{B}_2$  comprising 89.15 wt % of the sample. Visual inspection of the observed and predicted profiles reveals an excellent fit (Figure S8), confirming that  $\text{MgCo}_3\text{B}_2$  has been prepared in high yield and validating the structural model from SCXRD. Cell parameters from the refinement, together with the refined weight percent of identified impurity phases, are listed in Table S6.

**Comparison of  $\text{MgCo}_3\text{B}_2$  with Related Structure Types.** In Figure S9, bond lengths and interatomic separations of  $\text{MgCo}_3\text{B}_2$  and  $\text{MgNi}_3\text{B}_2$ <sup>24</sup> are compared. In all cases, distances between comparable atoms are remarkably similar. The only essential difference between the two types is that for the chiral  $\text{MgNi}_3\text{B}_2$  structure, Ni atoms with the same  $z$ -coordinate are never found adjacent to each other in the rumpled Kagomé network, while for  $\text{MgCo}_3\text{B}_2$  a Co1–Co1 or Co2–Co2 bond of 2.442 Å is statistically possible due to the disorder. This bond distance is slightly on the shorter side but not unreasonable for both Co–Co and Ni–Ni bonding.

It may well be asked why  $\text{MgCo}_3\text{B}_2$  does not simply adopt one of the ordered structure types known for other Mg- or Co-containing analogs.  $\text{RCO}_3\text{B}_2$  ternary compounds have been reported for  $R = \text{Sc}, \text{Y}, \text{Ce}, \text{Sm}, \text{Gd}, \text{Tb}, \text{Dy}, \text{Ho}, \text{Er}, \text{Tm}, \text{Yb}$ , and  $\text{Lu}$ , all of which are reported to crystallize in the prototypical  $\text{CeCo}_3\text{B}_2$  structure type featuring isolated B atoms rather than dimers.<sup>53,56</sup> The  $R$  metals in  $\text{RCO}_3\text{B}_2$  have +3 as a common oxidation state, while Mg exhibits a +2 oxidation state. Supposing that electron transfer occurs from  $M$  to the T–B framework in  $MT_3\text{B}_2$  compounds,  $R$  can donate up to 3 electrons in  $\text{RCO}_3\text{B}_2$  (for all  $R$  except Ce), so B atoms tend to isolate from each other. On the other hand, in  $\text{MgCo}_3\text{B}_2$ ,  $\text{MgNi}_3\text{B}_2$ , and  $\text{LiNi}_3\text{B}_{1.8}$ , the electropositive element only contributes up to one or two electrons to the T–B framework, so B atoms are more prone to form dimers to share electrons. For  $\text{ZrCo}_3\text{B}_2$ , the nominal oxidation state  $\text{Zr}^{4+}$  implies strong electron donating ability, which should lead to isolated B atoms. However, Zr has lower electron-donating ability compared to the rare-earth elements because of a stronger tendency to form localized covalent bonds. This is confirmed by Bader charge analysis on  $\text{MgNi}_3\text{B}_2$  and  $\text{ZrCo}_3\text{B}_2$ , indicating  $\text{Mg}^{1.54+}$  and  $\text{Zr}^{1.53+}$  Bader charges, respectively (see Table S7). Therefore, in terms of charge transfer, Zr behaves much like Mg in  $\text{ZrCo}_3\text{B}_2$ , so with fewer electrons available to the T–B framework, the formation of B–B dimers is observed.

**DFT Assessment of  $\text{MgCo}_3\text{B}_2$  Formation Energy.** Since electronic structure calculations for compounds exhibiting structural disorder are not straightforward, the formation energies for composition  $\text{MgCo}_3\text{B}_2$  were obtained for the three ordered structure types shown in Figure 3 ( $\text{CeCo}_3\text{B}_2$ ,  $\text{MgNi}_3\text{B}_2$ , and  $\text{ZrCo}_3\text{B}_2$ ). The DFT calculations were first performed using unrelaxed structures where unit cell parameters  $a = 4.89240$  Å and  $c = 2.93113$  Å (as refined from HR-PXRD data) were adapted to the three structure types of interest (using the relationships listed in the Supporting Information) while atomic coordinates were taken from reported models obtained using SCXRD for  $\text{CeCo}_3\text{B}_2$ ,  $\text{MgNi}_3\text{B}_2$ , and  $\text{ZrCo}_3\text{B}_2$ .<sup>24,53,54</sup> In addition, formation energies were calculated after DFT relaxation was performed for all three models (Table 2). Before relaxation, the  $\text{MgNi}_3\text{B}_2$  structure type was calculated to be the most energetically favorable, but after relaxation, the  $\text{ZrCo}_3\text{B}_2$

**Table 2. DFT Formation Energies for  $\text{MgCo}_3\text{B}_2$  with and without DFT Relaxation in Three Different Structure Types<sup>a</sup>**

structure type	magnetic ordering	formation energy (unrelaxed) (eV/f.u.)	formation energy (relaxed) eV/f.u.
$\text{CeCo}_3\text{B}_2$	NM <sup>b</sup>	-37.5675	-37.7282
$\text{MgNi}_3\text{B}_2$	NM <sup>b</sup>	-37.7142	-37.7510
	AFM		-37.7485
	FM		-37.7467
$\text{ZrCo}_3\text{B}_2$	NM	-37.4107	-37.7671
	FM <sup>b</sup>		-37.7676

<sup>a</sup>Spin-polarized DFT calculations reveal various relaxed structures with different magnetic order. NM = non-magnetic (paramagnetic or diamagnetic), FM = ferromagnetic, AFM = antiferromagnetic.

<sup>b</sup>Ground state.

structure type was found to be slightly more favorable, although the formation energies for all three structure types are much closer after relaxation. For the cases of  $\text{MgNi}_3\text{B}_2$  and  $\text{ZrCo}_3\text{B}_2$ , the cell volume decreased slightly; this is expected since DFT calculations model energetic behavior at 0 K. The  $\text{MgNi}_3\text{B}_2$ -type structure did not change substantially with the DFT relaxation, as evinced by the relatively slight change in energy during relaxation. The  $\text{ZrCo}_3\text{B}_2$ -type structure changed most significantly after the relaxation. Before relaxation, the B dimers displayed a bond distance of 1.713 Å and were twisted slightly out of the *ac*-, *bc*-, and other symmetry-related planes. After relaxation, the B atoms were found to lie within these planes, which allowed the structure to be described in higher symmetry group  $\bar{R}\bar{3}m$  (#166) as determined using FIND-SYM,<sup>57,58</sup> and the B–B distance increased to 1.874 Å, much closer to the experimental value of 1.870 Å (Figure S10). A previous computational study also found that DFT optimization caused the experimental  $\bar{R}\bar{3}$  structure of  $\text{ZrCo}_3\text{B}_2$  to relax to higher-symmetry  $\bar{R}\bar{3}m$  model.<sup>59</sup>

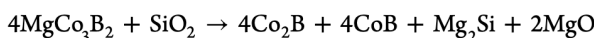
After relaxation, the  $\text{CeCo}_3\text{B}_2$ -type structure is the least energetically preferred. The substantial change in energy between unrelaxed and relaxed structures is due to a change in unit cell parameters:  $a$  increases from 4.89240 to 5.08131 Å while  $c$  decreases from 2.93110 to 2.72590 Å, with a relatively constant unit cell volume (60.758 Å<sup>3</sup> before vs 60.956 Å<sup>3</sup> after relaxation). This leads to a relative increase in bond distances within a single layer while distances between atoms in different layers decrease in length. In particular, the Co–Co distance increases from 2.442 Å, the separation that would be observed in a perfect Kagomé network with experimental unit-cell parameters, to 2.541 Å, which is slightly longer than the longest possible Co2–Co2 distance in the disordered structure, namely 2.536 Å. The Co–B distances are reduced from 2.035 to 2.002 Å, slightly shorter than any of the realistic Co–B bonds in the disordered structure. For  $\text{CeCo}_3\text{B}_2$ , the Co–Co distance is approximately 2.53 Å, and for other  $\text{RCO}_3\text{B}_2$  compounds it ranges from 2.47 to 2.54 Å. This observation suggests that another reason  $\text{MgCo}_3\text{B}_2$  does not adopt the ordered  $P6/mmm$  structure displayed by all the  $\text{RCO}_3\text{B}_2$  compounds is that a perfect Kagomé network of all Co atoms within the plane  $z = 0.5$  would force the atoms to move apart to achieve an optimal separation of ~2.5 Å. This would lead to an increase in the  $a$  cell parameter which would be compensated by a decrease in the  $c$  parameter to maintain reasonable Mg–Co and Mg–B spacing, permitted by the smaller ionic radius of Mg compared to R. The unit-cell

distortion of the DFT-relaxed  $\text{CeCo}_3\text{B}_2$  structure as well as its higher formation energy can be interpreted as suggesting that a flat network of Co atoms is not a favorable motif for  $\text{MgCo}_3\text{B}_2$ .

Additionally, Bader charge analysis performed for DFT-relaxed  $\text{MgCo}_3\text{B}_2$  in the  $\text{MgNi}_3\text{B}_2$  and  $\text{ZrCo}_3\text{B}_2$  structure types indicates effectively the same Bader charges for each atom type between the two structures. The charge assignment  $\text{Mg}^{1.55+}(\text{Co}^{0.25-})_3(\text{B}^{0.39-})_2$  shows that Mg exists in a fairly ionic state, while Co donates a small amount of electron density to B, as would be expected based on electronegativity values. These charges are also comparable to those determined for the structures of the  $\text{MgNi}_3\text{B}_2$  and  $\text{ZrCo}_3\text{B}_2$  compounds themselves (see Table S7).

As noted above, materials featuring a Kagomé network are known to exhibit exotic electronic, magnetic, and quantum properties. In materials with well-separated two-dimensional Kagomé networks, the electronic band structures often exhibit Dirac cones and flat bands. For the disordered  $\text{MgCo}_3\text{B}_2$  model as well as for the ordered, DFT-relaxed  $\text{CeCo}_3\text{B}_2$ -type and  $\text{MgNi}_3\text{B}_2$ -type, and  $\text{ZrCo}_3\text{B}_2$ -type models of  $\text{MgCo}_3\text{B}_2$ , the distance between Co atoms in adjacent Kagomé layers is similar to the distance between Co atoms within the Kagomé layer. In addition, the ratio between the shortest Co–Co separation within the Kagomé layer and the distance between a Co atom and its nearest neighbor (in this case, B) is 1.20. This means that the Co network in  $\text{MgCo}_3\text{B}_2$  is classified as a “semi-interacting Kagomé” network in contrast to an “isolated Kagomé network” as manifested in compounds such as  $\text{LiCo}_6\text{Ge}_6$ .<sup>29</sup> In the “semi-interacting Kagomé” networks, the Kagomé electronic bands are distorted by interactions with atoms not part of the Kagomé network, so characteristic Kagomé bands do not exist in these phases (Figures S11 and S12). Both nonspin-polarized and spin-polarized electronic structure calculations show metallic behavior for  $\text{MgCo}_3\text{B}_2$  in both ordered structure types, with no indication of exotic band structure features characteristic of a compound containing an isolated Kagomé network.

**Thermal Stability of  $\text{MgCo}_3\text{B}_2$ .** The high-temperature stability of a sample of  $\text{MgCo}_3\text{B}_2$  sealed under vacuum in a capillary was evaluated by means of temperature-resolved synchrotron powder X-ray diffraction up to 1169 K (Figure 5a). Although trace impurities of Mg and  $\text{Co}_2\text{B}$  were present in the sample before heat treatment, their levels remained consistent up to 992 K, aside from the melting of Mg at 888 K. Above 992 K, the fraction of  $\text{Co}_2\text{B}$  gradually begins to increase and peaks for  $\text{CoB}$  emerge, indicating that decomposition of the ternary phase has begun. This is consistent with synchrotron PXRD of in situ formation of  $\text{MgCo}_3\text{B}_2$ , where the ternary phase is observed to decompose into binary borides  $\text{Co}_2\text{B}$  and  $\text{CoB}$  above 1016 K. Presumably, in this case, Mg is also lost to a side reaction with the silica capillary, according to the reaction below:



However, the complete decomposition of  $\text{MgCo}_3\text{B}_2$  does not occur during the fast heating up to 1169 K employed in the temperature-resolved synchrotron PXRD experiment, and the ternary phase remains the major phase upon cooling.

In addition, differential scanning calorimetry data were collected for a sample of  $\text{MgCo}_3\text{B}_2$  sealed under vacuum (Figure 5b). The smooth curve suggests that gradual phase transformation takes place upon heating without substantial change in enthalpy within a narrow temperature range; this is

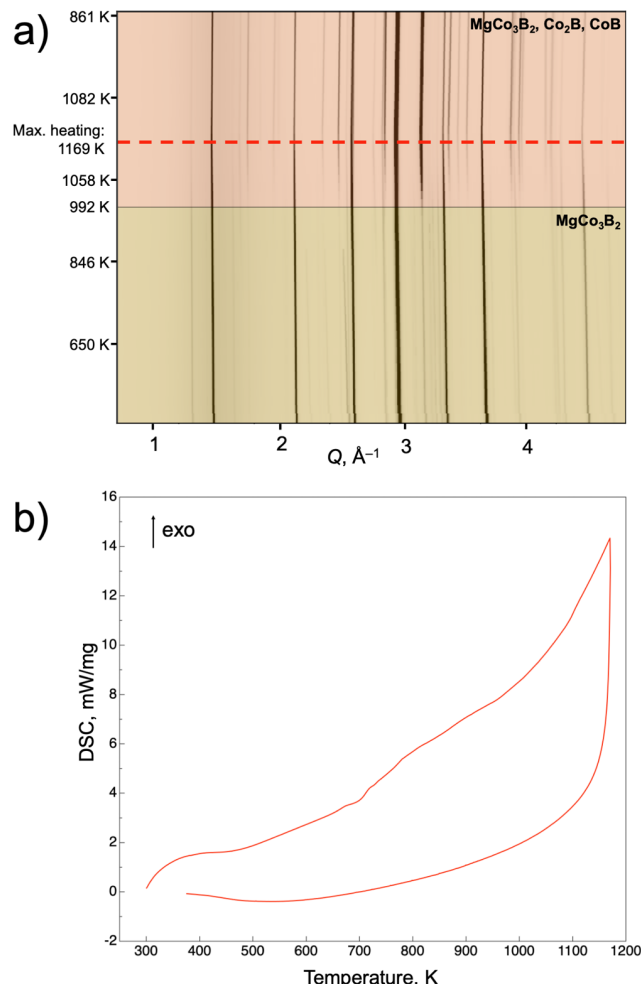


**Figure 5.** Thermal stability of  $\text{MgCo}_3\text{B}_2$ . (a) Temperature-resolved PXRD of a prereacted sample of  $\text{MgCo}_3\text{B}_2$ . Decomposition of the ternary phase into  $\text{Co}_2\text{B}$  and  $\text{CoB}$  begins at 992 K and continues gradually up to a maximum temperature of 1169 K. Initial and final PXRD patterns are compared with reference patterns for  $\text{MgCo}_3\text{B}_2$ ,  $\text{CoB}$ , and  $\text{Co}_2\text{B}$  in Figure S14. Data were collected at beamline 28-ID-2 NSLS-II BNL at wavelength  $\lambda = 0.1824$ . (b) Differential scanning calorimetry (DSC) measurement of  $\text{MgCo}_3\text{B}_2$  sealed under vacuum up to 1173 K.

consistent with the formation of binary compounds observed in the temperature-resolved PXRD data, where the fractions of  $\text{CoB}$  and  $\text{Co}_2\text{B}$  increase smoothly from 992 K to the maximum temperature of 1169 K and then remain constant at roughly 20–30 wt % each upon cooling down to 861 K. Because the ternary phase persists even at high temperatures, a sequential refinement of unit cell parameters as a function of temperature was possible (Table S8). Linear fitting of the temperature dependence of  $a$  and  $c$  parameters and cell volume data between 500 and 1000 K (Figure S13) gives coefficients of thermal expansion (CTE) according to the following equations:

$$\text{CTE}(a) = \frac{da}{dT} \times \frac{1}{a} = 1.52(1) \times 10^{-5} \text{ K}^{-1}$$

$$\text{CTE}(c) = \frac{dc}{dT} \times \frac{1}{c} = 1.301(9) \times 10^{-5} \text{ K}^{-1}$$

$$\text{CTE}(V) = \frac{dV}{dT} \times \frac{1}{V} = 4.39(3) \times 10^{-5} \text{ K}^{-1}$$

To investigate the stability of the  $\text{MgCo}_3\text{B}_2$  phase in air, a small amount ( $\sim 10$  mg) was placed in an open alumina crucible and heated to 973 K. Comparison of the PXRD patterns before and after heat treatment does not give any indication of decomposition of the ternary phase but rather reveals a reduction in the fraction of a Mg impurity present in the initial sample, most likely due to Mg evaporation and/or oxidation to form  $\text{MgO}$ . However, a longer dwell at 1173 K leads to the complete decomposition of the ternary phase into CoB and  $\text{Co}_2\text{B}$ , as well as  $\text{MgO}$  and  $\text{CoO}$ . PXRD patterns for these two tests are compared with that of the original sample in Figure S15.

**Magnetic Properties of  $\text{MgCo}_3\text{B}_2$ .** A polycrystalline powder sample of  $\text{MgCo}_3\text{B}_2$  synthesized from magnesium hydride was used for magnetic property measurements. According to Rietveld refinement of laboratory PXRD data for this sample, 83 wt % of the sample is composed of  $\text{MgCo}_3\text{B}_2$ , with 7–10 wt % impurities of Mg and  $\text{MgCo}_3(\text{B},\text{C})$ . Measurements of temperature-dependent magnetization of  $\text{MgCo}_3\text{B}_2$  at a low field of 1 kOe revealed a small positive magnetic susceptibility, suggesting bulk paramagnetism, with a non-Curie–Weiss temperature dependence (Figure S16). The presence of a small impurity ( $\sim 0.1$  wt %) of  $\text{MgB}_2$  ( $T_c = 39$  K) is inferred from a decrease in susceptibility below 36 K (Figure S16) and negative slope of magnetization at low field observed in the 5 K  $M(H)$  measurement (Figure S17).<sup>8</sup>

At high fields, the dependence of magnetization on field,  $M(H)$ , is linear at both 5 K (Figure S17) and 300 K (Figure 6b), consistent with bulk Pauli paramagnetism of the sample. At 300 K, a rapid increase in magnetization at low fields suggests a saturation of a ferromagnetic impurity. By fitting the data above 35 kOe with a linear fit and extrapolating to zero field, the magnitude of the saturation at 5 K was found to be  $9.2(2)$  emu/mol. Assuming this comes entirely from an impurity of  $\text{Co}_2\text{B}$ , this value corresponds to  $9.5 \times 10^{-4} \mu_{\text{B}}/\text{f.u.}$ , or about 0.06%  $\text{Co}_2\text{B}$  impurity given a moment of  $1.56 \mu_{\text{B}}/\text{f.u.}$  for  $\text{Co}_2\text{B}$  at 4.2 K.<sup>50</sup> Although the fraction of ferromagnetic impurity is small, the bulk paramagnetism of the sample gives a comparatively weak signal, so the small contribution from the saturation of Co moments is readily visible. Even though the content of the ferromagnetic impurity is only about 0.06%, as much as 6% of the magnetic response at 70 kOe can be attributed to this phase.

To evaluate the temperature-dependence of intrinsic magnetic susceptibility,  $M(T)$  was measured at 35 and 70 kOe, fields of sufficient strength to saturate the ferromagnetic impurity, and a Honda-Owen correction was applied to remove the contribution of this impurity (Figure 6a).<sup>61–63</sup>

$$\chi_{\text{corr}}(T) = \frac{M_{70 \text{ kOe}}(T) - M_{35 \text{ kOe}}(T)}{70 \text{ kOe} - 35 \text{ kOe}}$$

The inverse of susceptibility obtained via the Honda-Owen method was used for fitting with the modified Curie–Weiss equation:  $\chi_{\text{corr}}(T) = \chi_0 + C/(T - \theta)$ , where a temperature-independent term  $\chi_0$  accounts for Pauli paramagnetism of conduction electrons and the diamagnetic contributions of core electrons and the sample holder. The plot of  $\chi_{\text{corr}}^{-1}$  vs  $T$  is nearly linear from 15 to 300 K (inset to Figure 6a). However, the modified Curie–Weiss equation does not give an adequate fit over the entire range owing to slight irregularities in the

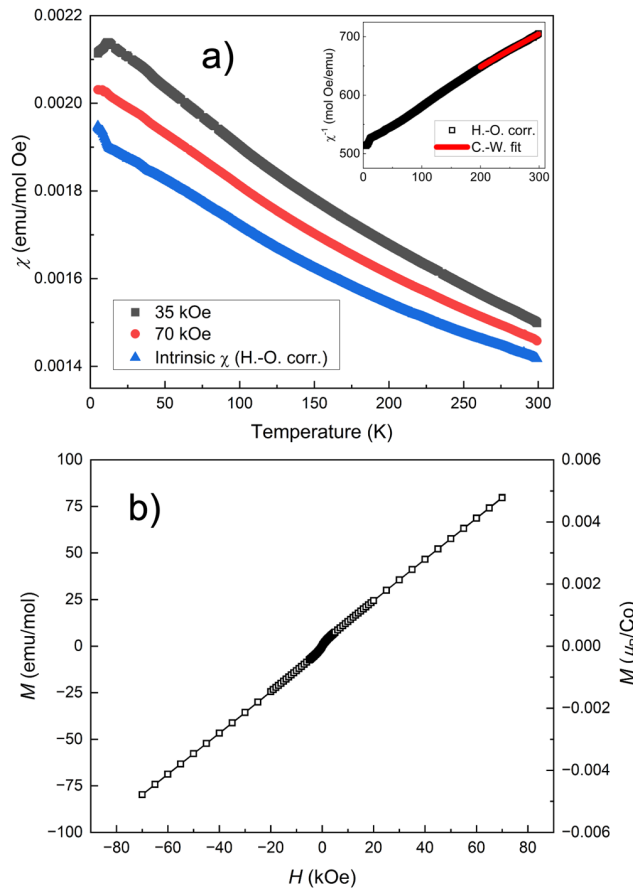


**Figure 6.** (a) Measured susceptibility  $\chi(T)$  at 35 kOe (gray) and 70 kOe (red) fields, and intrinsic susceptibility  $\chi_{\text{corr}}(T)$  obtained using the Honda-Owen method to correct for a trace amount of ferromagnetic impurity; inset: fit of inverse susceptibility ( $\chi_{\text{corr}}^{-1}$ ) between 200 and 300 K with the modified Curie–Weiss equation yielding fitted parameters  $\chi_0 = 6.2(2) \times 10^{-4}$  emu/mol Oe,  $C = 0.59(3)$  emu K/mol Oe, and  $\theta = -443(16)$  K. (b) Isothermal  $M(H)$  at 300 K, with a small saturation at low field indicative of a ferromagnetic impurity.

inflection of the curve. Moreover, the parameters of the Curie–Weiss fit depend strongly on the temperature range used for the fitting, most likely a consequence of a substantial temperature-independent term. In fitting selected data in ranges between 100 and 300 K, a remarkably large magnitude for the Weiss constant  $\theta$  between  $-500$  and  $-200$  K is obtained with a considerable contribution from the temperature-independent term  $\chi_0$  ranging between  $5 \times 10^{-4}$  and  $9 \times 10^{-4}$  emu/mol Oe, while the Curie constant  $C$  is found between 0.3 and 0.7 emu K/mol Oe (inset to Figure 6a). The considerable contribution from the temperature-independent term to the total magnitude of susceptibility indicates Pauli paramagnetism, in agreement with the other paramagnetic  $\text{MCo}_3\text{B}_2$  compounds (vide infra) and the metallic nature of  $\text{MgCo}_3\text{B}_2$ . The large magnitude of the Weiss constant can point to magnetic frustration or spin-glass behavior but can also indicate that a Curie–Weiss fit is not suitable for the data due to a substantial temperature-independent contribution to the total susceptibility.<sup>64,65</sup> It should be noted that ZFC/FC splitting of  $\chi$  at low temperatures, if present, would be difficult to observe since below 39 K the strong diamagnetism of superconducting  $\text{MgB}_2$  dominates the measurement. Further-

more, the *ac* susceptibility measured at three different frequencies in a 1000 Oe *dc* bias field in the range 2–50 K (**Figures S18 and S19**) is dominated by the contribution from the MgB<sub>2</sub> impurity since the real component of *ac* susceptibility decreases below the superconducting transition temperature of MgB<sub>2</sub> (**Figure S18**).

It may be insightful to compare the magnetic properties of MgCo<sub>3</sub>B<sub>2</sub> with other members of the MCo<sub>3</sub>B<sub>2</sub> family. Most of the reported MCo<sub>3</sub>B<sub>2</sub> compounds include a rare-earth element in the *M* site. Of those for which magnetic susceptibility has been measured over a range of temperatures, the Gd, Dy, Tb, and Ho compounds exhibit a ferromagnetic transition between 10 and 60 K with Curie–Weiss behavior above the transition;<sup>66–69</sup> the Sm compound features a potential ferrimagnetic transition at 43 K and Van Vleck paramagnetic behavior above the transition;<sup>66,70</sup> while the Y and Ce compounds appear to be Pauli (temperature-independent) paramagnets to the lowest measured temperatures.<sup>66,71,72</sup> In most of these cases, an anomaly is observed at 150–160 K, which is attributed variously to ordering or spin fluctuations of the Co sublattice<sup>73</sup> or a ferromagnetic impurity phase. In our analysis, the ubiquity of this feature, the variability in its relative intensity between samples of the same compound, as well as the low saturation moment reported for YCo<sub>3</sub>B<sub>2</sub> at 5 K<sup>66,71</sup> make the impurity explanation the most plausible. The measured intrinsic magnetic susceptibility (after Honda–Owen correction) for MgCo<sub>3</sub>B<sub>2</sub> is on the same order of magnitude compared to the reported values for paramagnetic YCo<sub>3</sub>B<sub>2</sub> and CeCo<sub>3</sub>B<sub>2</sub>, as well as susceptibility for SmCo<sub>3</sub>B<sub>2</sub>, GdCo<sub>3</sub>B<sub>2</sub>, and DyCo<sub>3</sub>B<sub>2</sub> arising only from the Co sublattice, estimated using the deviation from ideal Van Vleck or Curie–Weiss behavior (**Table 3**).<sup>66</sup> Comparison with ZrCo<sub>3</sub>B<sub>2</sub> and HfCo<sub>3</sub>B<sub>2</sub> would

**Table 3. Room-Temperature (300 K) or Temperature-Independent Contributions to the Magnetic Susceptibility of Various MCo<sub>3</sub>B<sub>2</sub> Compounds<sup>a</sup>**

	susceptibility (measured) (emu/mol Oe)	Co-sublattice susceptibility (calculated) (emu/mol Oe)
MgCo <sub>3</sub> B <sub>2</sub>	$1.42 \times 10^{-3}$	
YCo <sub>3</sub> B <sub>2</sub>	$3.5 \times 10^{-3}$	
CeCo <sub>3</sub> B <sub>2</sub>	$5.42 \times 10^{-4}$	
SmCo <sub>3</sub> B <sub>2</sub>		$3.8 \times 10^{-4}$
GdCo <sub>3</sub> B <sub>2</sub>		$7.1 \times 10^{-4}$
DyCo <sub>3</sub> B <sub>2</sub>		$1.4 \times 10^{-3}$

<sup>a</sup>For MgCo<sub>3</sub>B<sub>2</sub> (this work),  $\chi$  at 300 K (after Honda–Owen correction) is given; for YCo<sub>3</sub>B<sub>2</sub>,  $\chi$  at 300 K is estimated from a plot of  $\chi$  vs.  $T$ ,<sup>73</sup> while for the remaining compounds, the paramagnetic contributions are converted from reported values that are assumed to be temperature-independent.<sup>66,72</sup>

likely be insightful since Zr and Hf, like Mg, are not expected to contribute to the magnetic response of the ternary phase. In addition, these are the only other MCo<sub>3</sub>B<sub>2</sub> compounds where *M* is not a rare-earth metal, the Co Kagomé network is rumpled, and B–B dimers exist. Unfortunately, magnetic data on these compounds do not seem to be available.

To explore the energetic favorability of magnetic ordering in MgCo<sub>3</sub>B<sub>2</sub> in two ordered structure types, band structures were calculated for the CeCo<sub>3</sub>B<sub>2</sub> and MgNi<sub>3</sub>B<sub>2</sub> structure types using spin-polarized DFT after structural relaxation (**Table 2**). For MgCo<sub>3</sub>B<sub>2</sub> in the CeCo<sub>3</sub>B<sub>2</sub> and the MgNi<sub>3</sub>B<sub>2</sub> structure types, the DFT predicted ground state appears to be nonmagnetic,

i.e., no ordering of local magnetic moments. However, unusual low-lying excited metastable ferromagnetic and antiferromagnetic states were found with only slightly higher formation energies (see **Table 2**). For the ferromagnetic structure, spin-polarized DFT calculations predict a moment of 0.17  $\mu_B$ /Co1 atom and 0.41  $\mu_B$ /Co2 atom for an average of 0.33  $\mu_B$ /Co across the two Co sites. For the antiferromagnetic structure used for calculations, parallel ordering of spins within a single Co Kagomé layer and antiparallel ordering between adjacent layers (collinear spins) was considered. Antiferromagnetic states with noncollinear spins as predicted for some Kagomé compounds with noninteracting layers were not practical to consider using full-potential DFT in VASP. The predicted metastable collinear states should be taken with some caution as DFT does not take into account spin fluctuations (zero-point motion). The energy of these spin fluctuations is typically >10 meV/atom,<sup>74</sup> which is much larger than the obtained magnetic stabilization energies of our system (<1 meV/atom). In addition, disordered structures (including possible paramagnetic local moment structures) were not considered, and the extent to which conclusions can be drawn regarding the magnetic nature of MgCo<sub>3</sub>B<sub>2</sub> is limited. Nevertheless, the nonmagnetic ground state of MgCo<sub>3</sub>B<sub>2</sub> at  $T = 0$  K from the DFT calculations ultimately supports the experimentally observed non-Curie–Weiss behavior of susceptibility. The evidence presented herein cannot eliminate the possibility of antiferromagnetic order occurring above room temperature or a frustrated/spin glass state. Further investigation into the magnetic nature of this phase, including high-temperature magnetometry, <sup>11</sup>B solid-state NMR, magnetic Pair Distribution Function (PDF), heat capacity, and crystal growth could shed light on the intrinsic magnetic nature of this new boride.

## CONCLUSIONS

Guided by *in situ* diffraction to probe the mechanism of solid-state reactions and DFT predictions of structure stability, the synthesis of a new intermetallic ternary boride MgCo<sub>3</sub>B<sub>2</sub> has been accomplished using a magnesium hydride precursor MgH<sub>2</sub>. MgCo<sub>3</sub>B<sub>2</sub> is the first ternary compound reported in the Mg–Co–B system, adding another member to MT<sub>3</sub>B<sub>2</sub> family of intermetallic borides. Although the hydride route allows the solid-state reaction to proceed more quickly due to the intimate mixing of reactive precursors, synthesis with equivalent yield can be achieved with an elemental Mg precursor; the latter route was used to grow a crystal of MgCo<sub>3</sub>B<sub>2</sub> for structural characterization. The structure of MgCo<sub>3</sub>B<sub>2</sub> is a disordered variant of the CeCo<sub>3</sub>B<sub>2</sub> structure type, featuring a covalent framework that hosts Mg ions in its channels. The disorder associated with Co and B split sites leads to a rumpling of the Co Kagomé network and covalent B–B dimers, structural motifs uncharacteristic of the CeCo<sub>3</sub>B<sub>2</sub> prototype. Such bonding motifs of the MgCo<sub>3</sub>B<sub>2</sub> phase are very similar to those of chiral intermetallic MgNi<sub>3</sub>B<sub>2</sub>, but no indications of an ordered superstructure were found in the single-crystal or high-resolution powder diffraction experiments. In-situ X-ray diffraction allowed us to pinpoint an optimal synthesis temperature of 1023 K and showed that the formation of the ternary phase proceeds via an intermediate of Mg<sub>6</sub>Co<sub>2</sub>H<sub>11</sub>. Magnetic measurements revealed low magnetization with a weak temperature dependence, consistent with the considerable contribution of the temperature-independent

term of a Curie–Weiss fit and the predicted metallic and nonmagnetic ground state from DFT calculations.

This work highlights the utility of a multifaceted approach to the discovery of new solids in previously empty phase spaces. Crucial to this approach is the use of Rietveld analysis in examining *in situ* PXRD data collected upon heating of precursors mixture to identify peaks corresponding to potentially new compounds, as well as DFT assessment of their stability. *In situ* reaction monitoring provides direction as to the temperature range favorable for synthesis. Optimization of synthesis parameters is enabled by the rapid, diffusion-enhanced hydride route to provide essential experimental validation of a compound's stability via high-yield *ex situ* synthesis, while single crystal XRD in combination with synchrotron PXRD permitted accurate structure determination. Future studies will use this complex approach to screen for other ternary compounds in this and similar systems in search of new borides with distinctive magnetic properties.

## ■ ASSOCIATED CONTENT

### Supporting Information

The Supporting Information is available free of charge at <https://pubs.acs.org/doi/10.1021/acs.chemmater.4c01999>.

Additional tables with parameters of XRD data collection and refinement, tables and plots of PXRD phase analysis, additional structural information and graphics, results of DFT calculations, and additional magnetic measurements ([PDF](#))

$\text{MgCo}_3\text{B}_2$  crystallographic information ([CIF](#))

## ■ AUTHOR INFORMATION

### Corresponding Author

Julia V. Zaikina – Department of Chemistry, Iowa State University, Ames, Iowa 50011, United States;  [orcid.org/0000-0002-8755-1926](https://orcid.org/0000-0002-8755-1926); Email: [yzaikina@iastate.edu](mailto:yzaikina@iastate.edu)

### Authors

Paul Oftedahl – Department of Chemistry, Iowa State University, Ames, Iowa 50011, United States

Nawsher J. Parvez – Department of Physics and Astronomy, University of Delaware, Newark, Delaware 19716, United States

Zhen Zhang – Department of Physics and Astronomy, Iowa State University, Ames, Iowa 50011, United States;  [orcid.org/0009-0001-0810-8054](https://orcid.org/0009-0001-0810-8054)

Yang Sun – Department of Physics, Xiamen University, Xiamen 361005, China

Vladimir Antropov – Department of Physics and Astronomy, Iowa State University, Ames, Iowa 50011, United States; U.S. Department of Energy, Ames National Laboratory, Ames, Iowa 50011, United States

John Q. Xiao – Department of Physics and Astronomy, University of Delaware, Newark, Delaware 19716, United States;  [orcid.org/0000-0001-7805-8155](https://orcid.org/0000-0001-7805-8155)

Complete contact information is available at:

<https://pubs.acs.org/10.1021/acs.chemmater.4c01999>

### Funding

Financial support from the U.S. Department of Energy (DOE) Established Program to Stimulate Competitive Research (EPSCoR) Grant No. DE-SC0024284 is gratefully acknowledged. The Ames Laboratory is operated for the U.S.

Department of Energy by Iowa State University under contract #DE-AC02-07CH11358. This research used resources of the Advanced Photon Source, a U.S. Department of Energy (DOE) Office of Science user facility operated for the DOE Office of Science by Argonne National Laboratory under Contract No. DE-AC02-06CH11357. This research used beamline 28-ID-2 of the National Synchrotron Light Source II, a U.S. Department of Energy (DOE) Office of Science User Facility operated for the DOE Office of Science by Brookhaven National Laboratory under Contract No. DE-SC0012704. Part of the research described in this paper was performed at the Canadian Light Source, a national research facility of the University of Saskatchewan, which is supported by the Canada Foundation for Innovation (CFI), the Natural Sciences and Engineering Research Council (NSERC), the Canadian Institutes of Health Research (CIHR), the Government of Saskatchewan, and the University of Saskatchewan.

### Notes

The authors declare no competing financial interest.

## ■ ACKNOWLEDGMENTS

We thank Dr. Wenqian Xu at beamline 17-BM APS ANL, Dr. Jianming Bai and Dr. Hui Zhong at 28-ID-2 NSLS-II BNL for assisting with the respective *in situ* data collection experiments. We also thank Dr. Adam Leontowich at WLE BXDS CLS for assistance with planning and completing the high-resolution powder X-ray diffraction experiment. We thank Prof. Kirill Kovnir (Chemistry, Iowa State University and Ames National Laboratory) for access to DSC and PXRD instruments and discussions; additionally, we are grateful to Dr. Arkady Ellern (Chemistry, Iowa State University) for assistance in collecting SCXRD data. We also thank Zhijie (Hugh) Chen and Prof. Kai Liu (Department of Physics, Georgetown University) for performing magnetic measurements.

## ■ REFERENCES

- (1) Akopov, G.; Yeung, M. T.; Kaner, R. B. Rediscovering the Crystal Chemistry of Borides. *Adv. Mater.* **2017**, *29*, No. 1604506.
- (2) Albert, B.; Hillebrecht, H. Boron: Elementary Challenge for Experimenters and Theoreticians. *Angew. Chem., Int. Ed.* **2009**, *2*, 8640–8668.
- (3) Fokwa, B. P. T. Borides: Solid-State Chemistry. In *Encyclopedia of Inorganic and Bioinorganic Chemistry*; Wiley: 2014; pp 1–14.
- (4) Park, H.; Encinas, A.; Scheifers, J. P.; Zhang, Y.; Fokwa, B. P. T. Boron-Dependency of Molybdenum Boride Electrocatalysts for the Hydrogen Evolution Reaction. *Angew. Chem. Int. Ed.* **2017**, *56*, 5575–5578.
- (5) Herbst, J. F.; Croat, J. J.; Pinkerton, F. E.; Yelon, W. B. Relationships between Crystal Structure and Magnetic Properties in  $\text{Nd}_2\text{Fe}_4\text{B}$ . *Phys. Rev. B* **1984**, *29* (7), 4176–4178.
- (6) Lamichhane, T. N.; Xiang, L.; Lin, Q.; Pandey, T.; Parker, D. S.; Kim, T. H.; Zhou, L.; Kramer, M. J.; Bud'Ko, S. L.; Canfield, P. C. Magnetic Properties of Single Crystalline Itinerant Ferromagnet  $\text{AlFe}_2\text{B}_2$ . *Phys. Rev. Mater.* **2018**, *2* (8), No. 084408.
- (7) Tan, X.; Chai, P.; Thompson, C. M.; Shatruk, M. Magnetocaloric Effect in  $\text{AlFe}_2\text{B}_2$ : Toward Magnetic Refrigerants from Earth-Abundant Elements. *J. Am. Chem. Soc.* **2013**, *135* (25), 9553–9557.
- (8) Nagamatsu, J.; Nakagawa, N.; Muranaka, T.; Zenitani, Y.; Akimitsu, J. Superconductivity at 39 K in Magnesium Diboride. *Nature* **2001**, *401*, 63–64.
- (9) Gabani, S.; Flachbart, K.; Siemensmeyer, K.; Mori, T. Magnetism and Superconductivity of Rare Earth Borides. *J. Alloys Compd.* **2020**, *821*, No. 153201.

- (10) Mori, T. Thermoelectric and Magnetic Properties of Rare Earth Borides: Boron Cluster and Layered Compounds. *J. Solid State Chem.* **2019**, *275*, 70–82.
- (11) Bhaskar, G.; Gvozdetskyi, V.; Carnahan, S. L.; Wang, R.; Mantravadi, A.; Wu, X.; Ribeiro, R. A.; Huang, W.; Rossini, A. J.; Ho, K. M.; Canfield, P. C.; Lebedev, O. I.; Zaikina, J. V. Path Less Traveled: A Contemporary Twist on Synthesis and Traditional Structure Solution of Metastable LiNi<sub>12</sub>B<sub>8</sub>. *ACS Materials Au* **2022**, *2*, 614.
- (12) Gvozdetskyi, V.; Bhaskar, G.; Batuk, M.; Zhao, X.; Wang, R.; Carnahan, S. L.; Hanrahan, M. P.; Ribeiro, R. A.; Canfield, P. C.; Rossini, A. J.; Wang, C. Z.; Ho, K. M.; Hadermann, J.; Zaikina, J. V. Computationally Driven Discovery of a Family of Layered LiNiB Polymorphs. *Angew. Chem. Int. Ed.* **2019**, *58* (44), 15855–15862.
- (13) Gvozdetskyi, V.; Hanrahan, M. P.; Ribeiro, R. A.; Kim, T. H.; Zhou, L.; Rossini, A. J.; Canfield, P. C.; Zaikina, J. V. A Hydride Route to Ternary Alkali Metal Borides: A Case Study of Lithium Nickel Borides. *Chem. – Eur. J.* **2019**, *25* (16), 4123–4135.
- (14) Stadelmaier, H. H.; Draughn, R. A.; Hofer, G. Die Struktur Der Ternären Boride Vom Chromkarbid-(Cr<sub>23</sub>C<sub>6</sub>)-Typ. *Z. Metallkd.* **1963**, *54* (11), 640–644.
- (15) Adeyemi, A. N.; Bhaskar, G.; Cox, T.; Hong, S.; Gvozdetskyi, V.; Zaikina, J. V. Hydride Precursors in Materials Synthesis. In *Comprehensive Inorganic Chemistry III*, 3rd ed.; Elsevier: 2023; Vol. 1–10, pp 128–146.
- (16) Mantravadi, A.; Gvozdetskyi, V.; Sarkar, A.; Mudryk, Y.; Zaikina, J. V. Exploring the A -V-Sb Landscape beyond AV<sub>3</sub>Sb<sub>5</sub>: A Case Study on the KV<sub>6</sub>Sb<sub>6</sub> Kagome Compound. *Phys. Rev. Mater.* **2023**, *7* (11), No. 115002.
- (17) Gvozdetskyi, V.; Wang, R.; Xia, W.; Zhang, F.; Lin, Z.; Ho, K. M.; Miller, G.; Zaikina, J. V. How to Look for Compounds: Predictive Screening and in Situ Studies in Na–Zn–Bi System. *Chem. – Eur. J.* **2021**, *27* (64), 15954–15966.
- (18) Kovnir, K. Predictive Synthesis. *Chem. Mater.* **2021**, *33*, 4835–4841.
- (19) Bhaskar, G.; Behera, R. K.; Gvozdetskyi, V.; Carnahan, S. L.; Ribeiro, R. A.; Oftedahl, P.; Ward, C.; Canfield, P. C.; Rossini, A. J.; Huang, W.; Zaikina, J. V. Breaking New Ground: MBene Route toward Selective Vinyl Double Bond Hydrogenation in Nitroarenes. *J. Am. Chem. Soc.* **2023**, *145* (50), 27459–27470.
- (20) Bhaskar, G.; Gvozdetskyi, V.; Batuk, M.; Wiaderek, K. M.; Sun, Y.; Wang, R.; Zhang, C.; Carnahan, S. L.; Wu, X.; Ribeiro, R. A.; Bud'ko, S. L.; Canfield, P. C.; Huang, W.; Rossini, A. J.; Wang, C. Z.; Ho, K. M.; Hadermann, J.; Zaikina, J. V. Topochemical Deintercalation of Li from Layered LiNiB: Toward 2D MBene. *J. Am. Chem. Soc.* **2021**, *143* (11), 4213–4223.
- (21) Wang, R.; Sun, Y.; Gvozdetskyi, V.; Zhao, X.; Zhang, F.; Xu, L. H.; Zaikina, J. V.; Lin, Z.; Wang, C. Z.; Ho, K. M. Theoretical Search for Possible Li-Ni-B Crystal Structures Using an Adaptive Genetic Algorithm. *J. Appl. Phys.* **2020**, *127* (9), No. 094902.
- (22) Sun, J.; Wang, R.; Ding, Z.; Zhang, X.; Zhang, Q.; Zhang, B.; Dong, H.; Wu, F. Layered Li-Co-B as a Low-Potential Anode for Lithium-Ion Batteries. *Inorg. Chem.* **2023**, *62* (21), 8136–8144.
- (23) Jung, W. Darstellung Und Kristallstruktur von MgNi<sub>2</sub>SB<sub>2</sub> und Li<sub>1.2</sub>Ni<sub>2.5</sub>B<sub>2</sub>. *Z. Naturforsch.* **1977**, *32b*, 1371–1374.
- (24) Manfrinetti, P.; Pani, M.; Dhar, S. K.; Kulkarni, R. Structure, Transport and Magnetic Properties of MgNi<sub>3</sub>B<sub>2</sub>. *J. Alloys Compd.* **2007**, *428* (1–2), 94–98.
- (25) Meschke, V.; Gorai, P.; Stevanović, V.; Toberer, E. S. Search and Structural Featurization of Magnetically Frustrated Kagome Lattices. *Chem. Mater.* **2021**, *33* (12), 4373–4381.
- (26) Wilson, S. D.; Ortiz, B. R. AV<sub>3</sub>Sb<sub>5</sub> Kagome Superconductors. *Nature Reviews Materials* **2024**, *9*, 420.
- (27) Ye, L.; Kang, M.; Liu, J.; Von Cube, F.; Wicker, C. R.; Suzuki, T.; Jozwiak, C.; Bostwick, A.; Rotenberg, E.; Bell, D. C.; Fu, L.; Comin, R.; Checkelsky, J. G. Massive Dirac Fermions in a Ferromagnetic Kagome Metal. *Nature* **2018**, *555* (7698), 638–642.
- (28) Li, M.; Wang, Q.; Wang, G.; Yuan, Z.; Song, W.; Lou, R.; Liu, Z.; Huang, Y.; Liu, Z.; Lei, H.; Yin, Z.; Wang, S. Dirac Cone, Flat Band and Saddle Point in Kagome Magnet YMn<sub>6</sub>Sn<sub>6</sub>. *Nat. Commun.* **2021**, *12* (1), 3129.
- (29) Jovanovic, M.; Schoop, L. M. Simple Chemical Rules for Predicting Band Structures of Kagome Materials. *J. Am. Chem. Soc.* **2022**, *144* (24), 10978–10991.
- (30) Toby, B. H.; Von Dreele, R. B. GSAS-II: The Genesis of a Modern Open-Source All Purpose Crystallography Software Package. *J. Appl. Crystallogr.* **2013**, *46* (2), 544–549.
- (31) Krause, L.; Herbst-Irmer, R.; Sheldrick, G. M.; Stalke, D. Comparison of Silver and Molybdenum Microfocus X-Ray Sources for Single-Crystal Structure Determination. *J. Appl. Crystallogr.* **2015**, *48* (1), 3–10.
- (32) Sheldrick, G. M. SHELXT - Integrated Space-Group and Crystal-Structure Determination. *Acta Crystallogr. A* **2015**, *71* (1), 3–8.
- (33) Sheldrick, G. M. Crystal Structure Refinement with SHELXL. *Acta Crystallogr. C Struct. Chem.* **2015**, *71*, 3–8.
- (34) Momma, K.; Izumi, F. VESTA 3 for Three-Dimensional Visualization of Crystal, Volumetric and Morphology Data. *J. Appl. Crystallogr.* **2011**, *44* (6), 1272–1276.
- (35) Chupas, P. J.; Chapman, K. W.; Kurtz, C.; Hanson, J. C.; Lee, P. L.; Grey, C. P. A Versatile Sample-Environment Cell for Non-Ambient X-Ray Scattering Experiments. *J. Appl. Crystallogr.* **2008**, *41* (4), 822–824.
- (36) Gamage, E. H.; Greenfield, J. T.; Unger, C.; Kamali, S.; Clark, J. K.; Harmer, C. P.; Luo, L.; Wang, J.; Shatruk, M.; Kovnir, K. Tuning Fe-Se Tetrahedral Frameworks by a Combination of [Fe(en)<sub>3</sub>]<sup>2+</sup> Cations and Cl-Anions. *Inorg. Chem.* **2020**, *59* (18), 13353–13363.
- (37) Kresse, G.; Furthmüller, J. Efficient Iterative Schemes for *Ab Initio* Total-Energy Calculations Using a Plane-Wave Basis Set. *Phys. Rev. B* **1996**, *54* (16), 11169–11186.
- (38) Perdew, J. P.; Burke, K.; Ernzerhof, M. Generalized Gradient Approximation Made Simple. *Phys. Rev. Lett.* **1996**, *77* (18), 3865–3868.
- (39) Blöchl, P. E. Projector Augmented-Wave Method. *Phys. Rev. B* **1994**, *50* (24), 17953–17979.
- (40) Monkhurst, H. J.; Pack, J. D. Special Points for Brillouin-Zone Integrations. *Phys. Rev. B* **1976**, *13* (12), 5188–5192.
- (41) Černý, R.; Bonhomme, F.; Yvon, K.; Fischer, P.; Zolliker, P.; Cox, D. E.; Hewat, A. Hexamagnesium Dicobalt Undecadeuteride Mg<sub>6</sub>Co<sub>2</sub>D<sub>11</sub>: Containing [CoD<sub>4</sub>]<sup>3-</sup> and [CoD<sub>5</sub>]<sup>4-</sup> Complex Anions Conforming to the 18-Electron Rule. *J. Alloys Compd.* **1992**, *187*, 233–241.
- (42) Gennari, F. C.; Castro, F. J. Formation, Composition and Stability of Mg-Co Compounds. *J. Alloys Compd.* **2005**, *396* (1–2), 182–192.
- (43) Yoshida, M.; Bonhomme, F.; Yvon, K.; Fischer, P. On the Composition and Structure of the Cubic δ-Phase in the Mg-Co-H System. *J. Alloys Compd.* **1993**, *190* (2), L45–L46.
- (44) Buschow, K. H. J.; Van Engen, P. G.; Jongebreur, R. Magneto-Optical Properties of Metallic Ferromagnetic Materials. *J. Magn Magn Mater.* **1983**, *38* (1), 1–22.
- (45) Curtarolo, S.; Setyawan, W.; Hart, G. L. W.; Jahnatek, M.; Chepulskii, R. V.; Taylor, R. H.; Wang, S.; Xue, J.; Yang, K.; Levy, O.; Mehl, M. J.; Stokes, H. T.; Demchenko, D. O.; Morgan, D. AFLOW: An Automatic Framework for High-Throughput Materials Discovery. *Comput. Mater. Sci.* **2012**, *58*, 218–226.
- (46) Jain, A.; Ong, S. P.; Hautier, G.; Chen, W.; Richards, W. D.; Dacek, S.; Cholia, S.; Gunter, D.; Skinner, D.; Ceder, G.; Persson, K. A. Commentary: The Materials Project: A Materials Genome Approach to Accelerating Materials Innovation. *APL Mater.* **2013**, *1*, No. 011002.
- (47) Kirklin, S.; Saal, J. E.; Meredig, B.; Thompson, A.; Doak, J. W.; Aykol, M.; Rühl, S.; Wolverton, C. The Open Quantum Materials Database (OQMD): Assessing the Accuracy of DFT Formation Energies. *NPJ. Comput. Mater.* **2015**, *1*, 15010.
- (48) Saal, J. E.; Kirklin, S.; Aykol, M.; Meredig, B.; Wolverton, C. Materials Design and Discovery with High-Throughput Density

- Functional Theory: The Open Quantum Materials Database (OQMD). *JOM* **2013**, *65* (11), 1501–1509.
- (49) Gates-Rector, S.; Blanton, T. The Powder Diffraction File: A Quality Materials Characterization Database. *Powder Diffr* **2019**, *34* (4), 352–360.
- (50) Villars, P.; Cenzual, K. *Pearson's Crystal Data—Crystal Structure Database for Inorganic Compounds*; ASM International: Materials Park, OH, USA, 2016.
- (51) Zagorac, D.; Muller, H.; Ruehl, S.; Zagorac, J.; Rehme, S. Recent Developments in the Inorganic Crystal Structure Database: Theoretical Crystal Structure Data and Related Features. *J. Appl. Crystallogr.* **2019**, *52*, 918–925.
- (52) Leeman, J.; Liu, Y.; Stiles, J.; Lee, S. B.; Bhatt, P.; Schoop, L. M.; Palgrave, R. G. Challenges in High-Throughput Inorganic Materials Prediction and Autonomous Synthesis. *PRX Energy* **2024**, *3* (1), No. 011002.
- (53) Kuz'ma, Yu. B.; Kripyakevich, P. I.; Bilonizhko, N. S. Crystal Structure of CeCo<sub>3</sub>B<sub>2</sub> and Analogous Compounds. *Dopovidi Akademii Nauk Ukrains'koi RSR, Seriya A: Fizyko-Tekhnichni ta Matematichni Nauki* **1969**, *31* (10), 939–941.
- (54) Voroshilov, Yu. V.; Kuz'ma, Yu. B. Reaction of Zirconium with the Transition Metals and Boron. *Soviet. Powder Metallurgy and Metal Ceramics* **1969**, *8* (11), 941–944.
- (55) Alekseeva, A. M.; Abakumov, A. M.; Chizhov, P. S.; Leithe-Jasper, A.; Schnelle, W.; Prots, Y.; Hadermann, J.; Antipov, E. V.; Grin, Y. Ternary Magnesium Rhodium Boride Mg<sub>2</sub>Rh<sub>1-x</sub>B<sub>6+2x</sub> with a Modified Y<sub>2</sub>ReB<sub>6</sub>-Type Crystal Structure. *Inorg. Chem.* **2007**, *46* (18), 7378–7386.
- (56) Rogl, P. Über SE-Metall - Kobaltboride. *Monatsh. Chem.* **1973**, *104* (6), 1623–1631.
- (57) Stokes, H. T.; Hatch, D. M. FINDSYM: Program for Identifying the Space-Group Symmetry of a Crystal. *J. Appl. Crystallogr.* **2005**, *38*, 237–238.
- (58) Stokes, H. T.; Hatch, D. M.; Campbell, B. J. FINDSYM, ISOTROPY Software Suite. [iso.byu.edu](http://iso.byu.edu).
- (59) Wu, S. Q.; Ji, M.; Wang, C. Z.; Nguyen, M. C.; Zhao, X.; Umemoto, K.; Wentzcovitch, R. M.; Ho, K. M. An Adaptive Genetic Algorithm for Crystal Structure Prediction. *J. Phys.: Condens. Matter* **2014**, *26* (3), No. 035402.
- (60) Kanomata, T.; Ise, Y.; Kumagai, N.; Haga, A.; Kamishima, K.; Goto, T.; Kimura, H. M.; Yoshida, H.; Kaneko, T.; Inoue, A. Magnetovolume Effect of Co<sub>2</sub>B. *J. Alloys Compd.* **1997**, *259* (1–2), L1–L4.
- (61) Owen, M. Magnetochemische Untersuchungen. Die Thermo-magnetischen Eigenschaften Der Elemente. *Ann. Phys.* **1912**, *342*, 657–699.
- (62) Honda, K. Die Thermomagnetischen Eigenschaften Der Elemente. *Ann. Phys.* **1910**, *337*, 1027–1063.
- (63) Yang, J.; Matsui, M.; Kawa, M.; Ohta, H.; Michioka, C.; Dong, C.; Wang, H.; Yuan, H.; Fang, M.; Yoshimura, K. Magnetic and Superconducting Properties in Single Crystalline Fe<sub>1+δ</sub>Te<sub>1-x</sub>Se<sub>x</sub> ( $x < 0.50$ ) System. *J. Phys. Soc. Jpn.* **2010**, *79* (7), No. 074704.
- (64) Mydosh, J. A. *Spin Glasses*, 1st ed., eBook; CRC Press: London, 2014.
- (65) Siebeneichler, S.; Ovchinnikov, A.; Sheptyakov, D.; Mudring, A. V. Making a Hedgehog Spin-Vortex State Possible: Geometric Frustration on a Square Lattice. *Chem. Mater.* **2024**, *36* (8), 3546–3554.
- (66) Ido, H.; Nanjo, M.; Yamada, M. Magnetic Susceptibility of RC<sub>o</sub><sub>3</sub>B<sub>2</sub> (R = Y, Sm, Gd, and Dy). *J. Appl. Phys.* **1994**, *75* (10), 7140–7142.
- (67) Caspi, E. N.; Dubman, M.; Ettedgui, H.; Shaked, H.; Short, S.; Jorgensen, J. D. Magnetic and Crystallographic Properties of HoCo<sub>3</sub>B<sub>2</sub>. *In Physica B: Condensed Matter* **2005**, *359–361*, 944–946.
- (68) Zheng, X. Q.; Xu, J. W.; Zhang, H.; Zhang, J. Y.; Wang, S. G.; Zhang, Y.; Xu, Z. Y.; Wang, L. C.; Shen, B. G. Magnetic Properties and Magnetocaloric Effect of HoCo<sub>3</sub>B<sub>2</sub> Compound. *AIP Adv.* **2018**, *8* (5), No. 056432.
- (69) Li, L.; Huo, D.; Igawa, H.; Nishimura, K. Large Magnetocaloric Effect in TbCo<sub>3</sub>B<sub>2</sub> Compound. *J. Alloys Compd.* **2011**, *509* (5), 1796–1799.
- (70) Ido, H.; Yamada, M.; Nashima, O.; Ito, T.; Yoshida, H. Anomalous Magnetic Properties of the Compound SmCo<sub>3</sub>B<sub>2</sub>. *J. Appl. Phys.* **2000**, *87* (9), 4912–4914.
- (71) Ching, W. Y.; Ido, H.; Yamauchi, H.; Cheng, S. F.; Sankar, S. G.; Wallace, W. E. Magnetism in Elements, Alloys, and Compounds Magnetic Properties of the Y<sub>1-x</sub>Gd<sub>x</sub>Co<sub>3</sub>B<sub>2</sub> System. *J. Appl. Phys.* **1991**, *70* (10), 6540–6542.
- (72) Yang, K. N.; Torikachvili, M. S.; Maple, M. B.; Ku, H. C. Magnetic Susceptibility of CeT<sub>3</sub>B<sub>2</sub> and UT<sub>3</sub>B<sub>2</sub> Compounds (T = Co, Ru, and Ir). *J. Appl. Phys.* **1985**, *57* (8), 3140–3142.
- (73) Ballou, R.; Burzo, E.; Pop, V. Magnetic Properties of (Gd<sub>x</sub>Y<sub>1-x</sub>)Co<sub>3</sub>B<sub>2</sub> Compounds. *J. Magn Magn Mater.* **1995**, *140–144*, 945–946.
- (74) Wysocki, A. L.; Valmispild, V. N.; Kutepov, A.; Sharma, S.; Dewhurst, J. K.; Gross, E. K. U.; Lichtenstein, A. I.; Antropov, V. P. Spin-Density Fluctuations and the Fluctuation-Dissipation Theorem in 3d Ferromagnetic Metals. *Phys. Rev. B* **2017**, *96* (18), No. 184418.

# Venturing into Unexplored Phase Space: Synthesis, Structure, and Properties of MgCo<sub>3</sub>B<sub>2</sub> Featuring a Rumpled Kagomé Network

Paul Oftedahl,<sup>a</sup> Nawsher J. Parvez,<sup>b</sup> Zhen Zhang,<sup>c</sup> Yang Sun,<sup>d</sup> Vladimir Antropov,<sup>c,e</sup> John Q. Xiao,<sup>b</sup> Julia V. Zaikina<sup>a\*</sup>

<sup>a</sup>Department of Chemistry, Iowa State University, Ames, Iowa 50011, United States

<sup>b</sup>Department of Physics and Astronomy, University of Delaware, Newark, Delaware 19716, United States

<sup>c</sup>Department of Physics and Astronomy, Iowa State University, Ames, Iowa 50011, United States

<sup>d</sup>Department of Physics, Xiamen University, Xiamen 361005, China

<sup>e</sup>Ames National Laboratory, U.S. Department of Energy, Ames, Iowa 50011, United States

## SUPPORTING INFORMATION

**Table S1.** Comparison of structure solutions from SCXRD at 210 K in space groups  $P\bar{3}$ ,  $P6/m$ , and  $P6/mmm$ . The non-standardized coordinates for the B site are reported to make clear its proximity to the site  $(x, 2x, z)$ , a  $6l$  site in  $P6/mmm$ .

$P\bar{3}$						
	$x/a$	$y/b$	$z/c$	s.o.f.	$U_{\text{eq}}$	Statistics
Co1 (3f)	0.5	0	0.5	0.324(7)	0.0063(3)	$wR_2$ 0.0537 $R_1$ 0.0240
Co2 (6g)	0.5002(3)	0.0002(3)	0.3821(9)	0.338(3)	0.0063	GoF 1.021 17 parameters
Mg (1a)	0	0	0	1	0.0094(2)	293 data
B (6g)	0.3900(9)	0.779(1)	0.002(2)	$\frac{1}{3}$	0.0061(5) <sup>a</sup>	
$P6/m$						
	$x/a$	$y/b$	$z/c$	s.o.f.	$U_{\text{eq}}$	Statistics
Co1 (3g)	0.5	0	0.5	0.323(7)	0.0064(4)	$wR_2$ 0.0512 $R_1$ 0.0213
Co2 (6i)	0.5	0	0.382(1)	0.339(4)	0.0064	GoF 1.066 12 parameters
Mg (1a)	0	0	0	1	0.0094(2)	169 data
B (6j)	0.390(1)	0.779(1)	0	$\frac{1}{3}$	0.0061(6)*	
$P6/mmm$						
	$x/a$	$y/b$	$z/c$	s.o.f.	$U_{\text{eq}}$	Statistics
Co1 (3g)	0.5	0	0.5	0.322(7)	0.0065(4)	$wR_2$ 0.0449 $R_1$ 0.0174
Co2 (6i)	0.5	0	0.382(1)	0.339(4)	0.0065	GoF 1.117 10 parameters
Mg (1a)	0	0	0	1	0.0095(3)	115 data
B (6l)	0.3894(6)	0.779(1)	0	$\frac{1}{3}$	0.0061(7)*	

<sup>a</sup>  $U_{\text{iso}}$  is used.

**Table S2.** Experimental details and crystallographic data for MgCo<sub>3</sub>B<sub>2</sub> from single-crystal diffraction experiment. Further details of the crystal structure refinement can be obtained from the Inorganic Crystal Structure Database (ICSD) from FIZ Karlsruhe – Leibniz Institute for Information Infrastructure ([www.fiz-karlsruhe.de](http://www.fiz-karlsruhe.de)) by quoting the CSD 2369299 deposition number at [www.ccdc.cam.ac.uk/structures](http://www.ccdc.cam.ac.uk/structures).

Empirical formula	MgCo <sub>3</sub> B <sub>2</sub>
Space group, <i>Z</i>	<i>P</i> 6/ <i>mmm</i> (#191), 1
Cell parameters: <i>a</i> , Å	4.883(2)
<i>c</i> , Å	2.926(2)
<i>V</i> , Å <sup>3</sup>	60.42(6)
Cell wt., amu	222.72
Crystal density, g cm <sup>-3</sup>	6.121
Temperature, K	210
Wavelength, Å	0.71073 (Mo <i>K<sub>a</sub></i> )
Absorption coeff., mm <sup>-1</sup>	20.21
Minimum/maximum transmission	0.5794/0.7489
Maximum $\theta$ , °	42.42
Range of <i>h</i> , <i>k</i> , <i>l</i>	±9, ±9, ±5
<i>F</i> (000)	103.0
Crystal size, mm	0.005 × 0.005 × 0.015
Measured reflections	4075
Rejected reflections ( $2\theta > 84.84^\circ$ )	402
Unique reflections possible	115
Unique reflections measured	115 ( <i>R</i> <sub>int</sub> = 0.0574)
# l.s. parameters	10
GoF for <i>F</i> <sup>2</sup>	1.117
<i>R</i> <sub>1</sub> (all data)	0.0248
<i>R</i> <sub>1</sub> [ <i>F</i> <sub>o</sub> > 4σ( <i>F</i> <sub>o</sub> )]	0.0174
<i>wR</i> <sub>2</sub>	0.0449
Weighting coefficients	0.0243, 0.00
Largest difference peak, e/Å <sup>3</sup>	1.31 <sup>a</sup>
Largest difference hole, e/Å <sup>3</sup>	-0.42

<sup>a</sup> A small electron density peak (1.31  $e^-$ ), more than twice as high as the next largest peak, was observed in the difference Fourier map. This peak is located exactly between the two Mg atoms along the *c*-axis at (0, 0, 0.5) and at 2.44 Å from neighboring Co atoms in the *z* = 0.5 plane. This distance is unrealistic for either Mg or B bonding to Co, so a third Co site (1*b*) was added and constrained such that the occupancies of the Mg atom in the 1*a* site and this Co atom sum to unity. Adding this atomic site eliminated the difference peak, and the *R* factors improved slightly: *R*<sub>1</sub> = 0.0164, *wR*<sub>2</sub> = 0.0389 compared to *R*<sub>1</sub> = 0.0174, *wR*<sub>2</sub> = 0.0449. However, the occupancy of Co in the 1*b* site was refined to 0.9(2)% , which is close to 0 within 3 estimated standard deviations. The high relative uncertainty together with low refined occupancy factor makes it unlikely to be a feature of crystal structure, therefore in the final stages of refinement this site was removed and the Mg site is refined as fully occupied.

**Table S3.** Refined atomic coordinates, occupancies, and anisotropic harmonic thermal displacement parameters for Co and Mg atoms as determined from SCXRD data at 210 K.

Atom	Wyckoff site	$x/a$	$y/b$	$z/c$	s.o.f.	$U_{\text{eq}}$
Co1	$3g$	0.5	0	0.5	0.322(7)	0.0065(4)
Co2	$6i$	0.5	0	0.382(1)	0.339(4)	0.0065
Mg1	$1a$	0	0	0	1	0.0095(3)
B1	$6l$	0.6106(6)	0.221(1)	0	$\frac{1}{3}$	0.0061(7) <sup>a</sup>

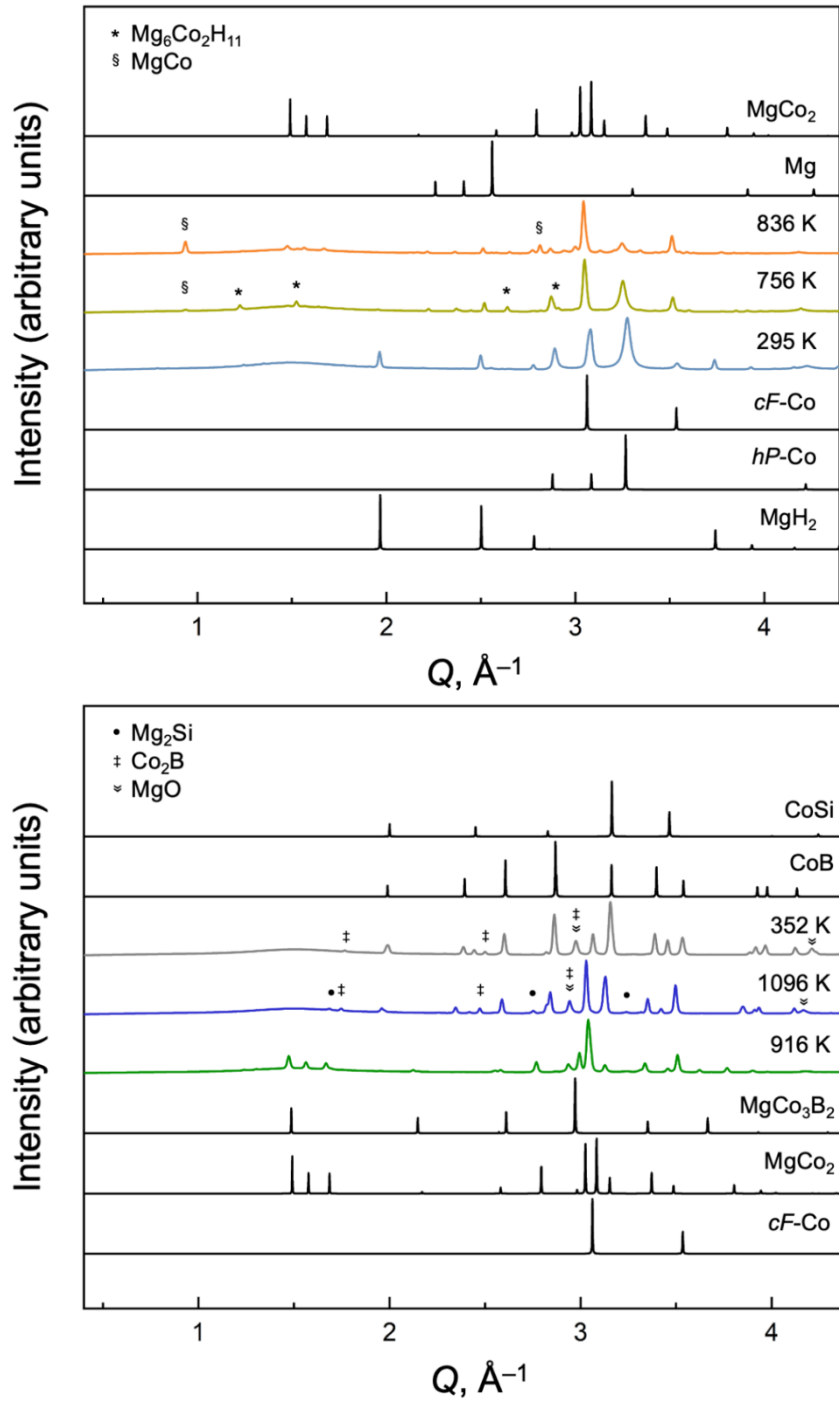
  

Atom	$U_{11}$	$U_{22}$	$U_{33}$	$U_{23}$	$U_{13}$	$U_{12}$
Co1	0.0062(1)	0.0048(1)	0.008(1)	0	0	0.00238(7)
Co2	0.0062(1)	0.0048(1)	0.008(1)	0	0	0.00238(7)
Mg1	0.0094(3)	0.0094(3)	0.0096(6)	0	0	0.0047(2)
B1	—	—	—	—	—	—

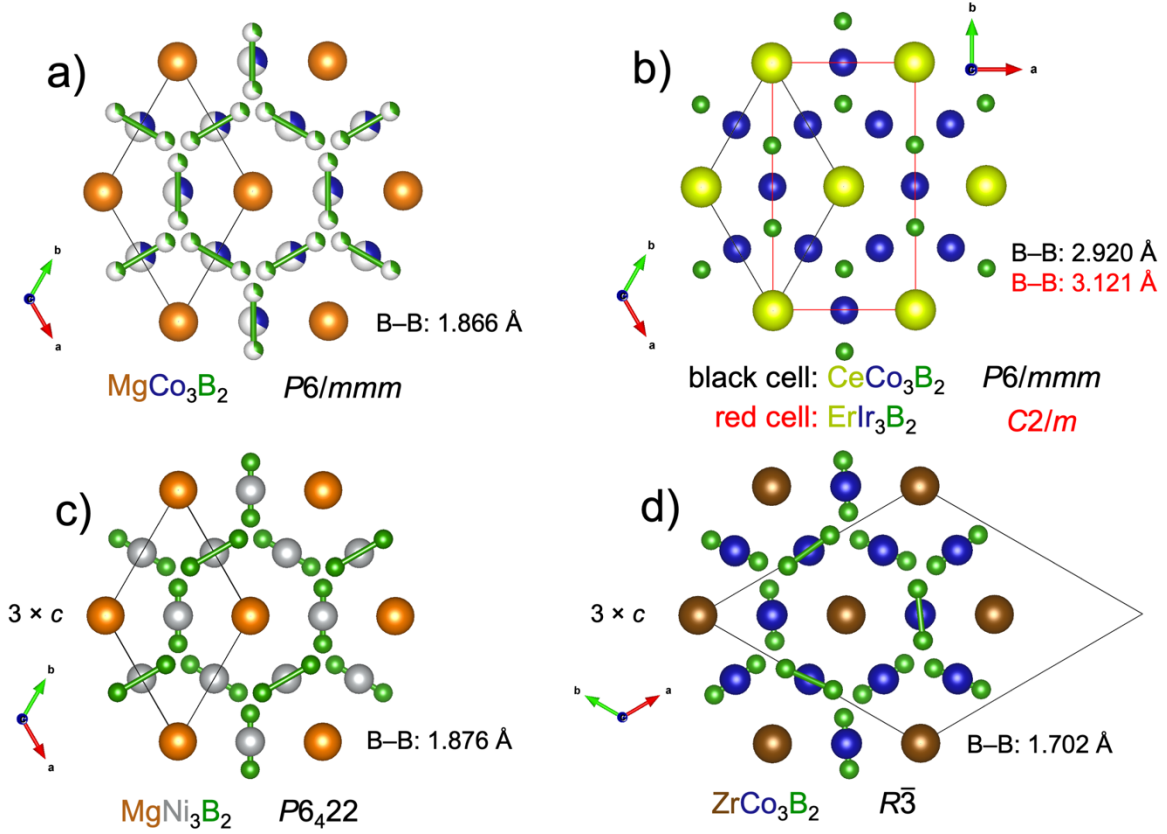
<sup>a</sup>  $U_{\text{iso}}$  is used.

**Table S4.** Rietveld refinement results of selected PXRD patterns obtained during in situ reaction of MgH<sub>2</sub>, Co, and B at beamline 17-BM APS ANL. Refinement was carried out using GSAS-II software,<sup>1</sup> and the only parameters refined were scale factor, phase fractions, background coefficients (~30-term Chebyshev polynomial), and unit cell parameters. The large number of background coefficients was used to account for a broad peak at low angles due to the silica capillary. Percentages listed are weight percent (wt. %), which were constrained to sum to 100% for each refinement. Structure models were taken from ICSD database:<sup>2</sup> MgH<sub>2</sub> [PDF-01-074-0934], *cF*-Co [PDF-01-090-5299], *hP*-Co [PDF-01-080-6668], Mg [PDF-01-080-4430], Mg<sub>6</sub>Co<sub>2</sub>H<sub>11</sub> [PDF-01-073-9701], MgCo<sub>2</sub> [PDF-01-082-6057], Mg<sub>2</sub>Si [PDF-01-074-5963], Co<sub>2</sub>B [PDF-01-090-5420], CoB [PDF-01-085-4540], MgO [PDF-01-090-2418], CoSi [PDF-01-082-9100], except for MgCo [PCD-451959], the model for which was found in Pearson's Crystal Data 2016/17.<sup>3</sup> An adapted structure model of MgNi<sub>3</sub>B<sub>2</sub> [PDF-01-075-8152] was used for MgCo<sub>3</sub>B<sub>2</sub>.

Frame	T, K	MgH <sub>2</sub>	<i>cF</i> -Co	<i>hP</i> -Co	Mg	Mg <sub>6</sub> Co <sub>2</sub> H <sub>11</sub>	MgCo	MgCo <sub>2</sub>	MgCo <sub>3</sub> B <sub>2</sub>	Mg <sub>2</sub> Si	Co <sub>2</sub> B	CoB	MgO	CoSi
18	656	26.5%	23.2%	45.6%	4.7%									
20	696	1.1%	29.2%	44.4%	20.7%	4.5%								
22	736		31.9%	37.1%	15.3%	15.7%								
23	756		34.3%	32.4%	13.4%	16.5%	1.2%	2.3%						
24	775		37.5%	28.8%	15.7%		12.0%	6.1%						
26	816		43.0%	15.6%	12.6%		15.5%	11.7%	1.6%					
28	856		42.8%	4.8%	6.0%		12.1%	28.4%	5.9%					
29	875		39.2%	1.8%			3.7%	45.7%	9.6%					
30	896		34.4%					53.9%	11.7%					
31	916		35.4%					52.1%	12.4%					
32	935		41.3%					46.5%	12.2%					
34	975		58.7%					21.8%	9.7%	4.4%	5.3%			
35	995		68.3%					8.1%	7.9%	4.7%	9.0%	1.9%		
36	1016		64.7%					4.3%	5.0%	13.9%	12.0%			
38	1056		40.8%						4.0%	17.2%	26.9%	11.1%		
40	1096		25.2%						2.3%	15.6%	39.2%	12.9%	4.8%	
42	1135		13.4%						0.7%	11.4%	49.0%	15.0%	10.5%	
49	352		8.7%							6.8%	47.7%	18.0%	18.8%	

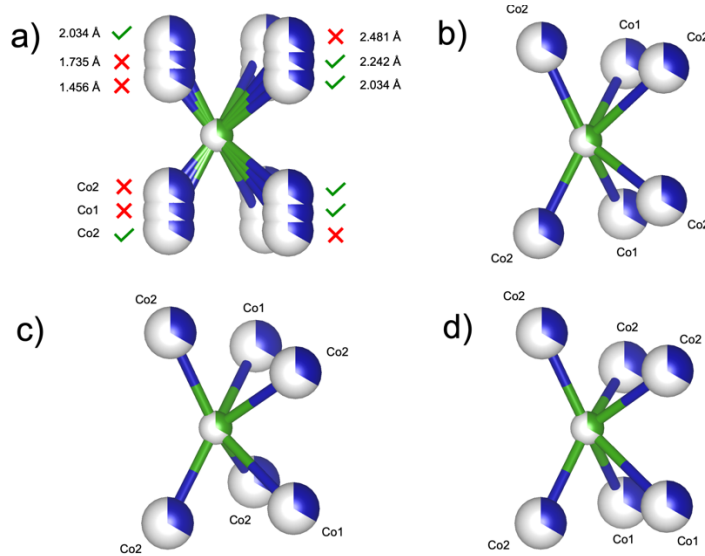


**Figure S1.** Phase analysis of representative powder X-ray diffraction patterns from each region of Figure 1. PXRD patterns in black are calculated patterns for the major phases in the experimental PXRD data; the colors of the experimental PXRD patterns correspond to the region of the waterfall plot in Figure 1 they are taken from. Diffraction peaks corresponding to minor phases are indicated by symbols referenced to a phase composition at the top left corner of each plot.

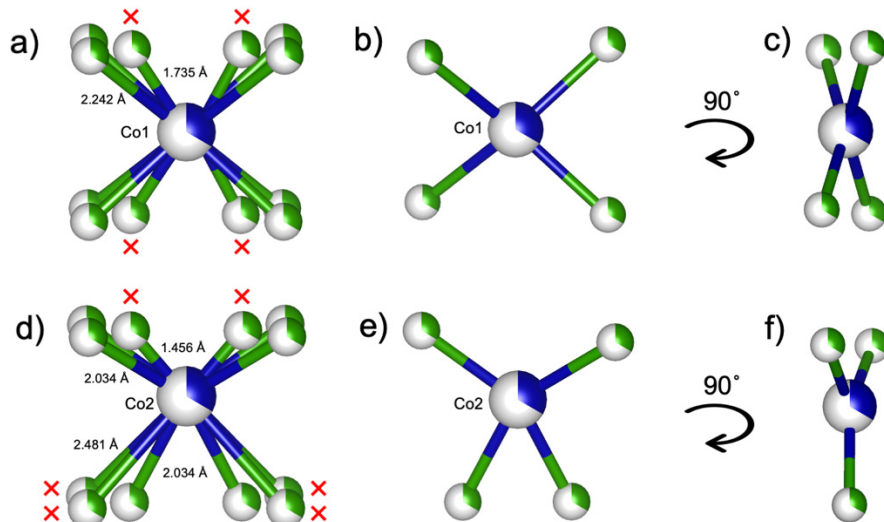


### Supplemental discussion to Figure 3 regarding unit cell relations.

Panel (a) of Figure 3 represents the small cell adopted by  $\text{MgCo}_3\text{B}_2$ ; this is the same cell shown in black in panel b for  $\text{CeCo}_3\text{B}_2$  and adopted by other  $RCo_3\text{B}_2$  structures.<sup>4</sup> The red cell in panel (b) represents a *C*-centered orthorhombic cell similar to the monoclinic cell found in the  $\text{ErIr}_3\text{B}_2$  structure type,<sup>5</sup> with  $a(\text{ErIr}_3\text{B}_2) = a(\text{CeCo}_3\text{B}_2)$ ,  $b(\text{ErIr}_3\text{B}_2) = \sqrt{3} \times b(\text{CeCo}_3\text{B}_2)$ ,  $c(\text{ErIr}_3\text{B}_2) = c(\text{CeCo}_3\text{B}_2)$ , and  $\beta \approx 90^\circ$ . Panel (c) shows the threefold supercell found for  $\text{MgNi}_3\text{B}_2$ ,<sup>6</sup> where  $c(\text{MgNi}_3\text{B}_2) = 3 \times c(\text{CeCo}_3\text{B}_2)$ , while panel (d) shows the rhombohedral cell (hexagonal settings) adopted by  $\text{ZrCo}_3\text{B}_2$ <sup>7</sup> with  $a(\text{ZrCo}_3\text{B}_2) = b(\text{ZrCo}_3\text{B}_2) = \sqrt{3} \times a(\text{CeCo}_3\text{B}_2)$  and  $c(\text{ZrCo}_3\text{B}_2) = 3 \times c(\text{CeCo}_3\text{B}_2)$ .



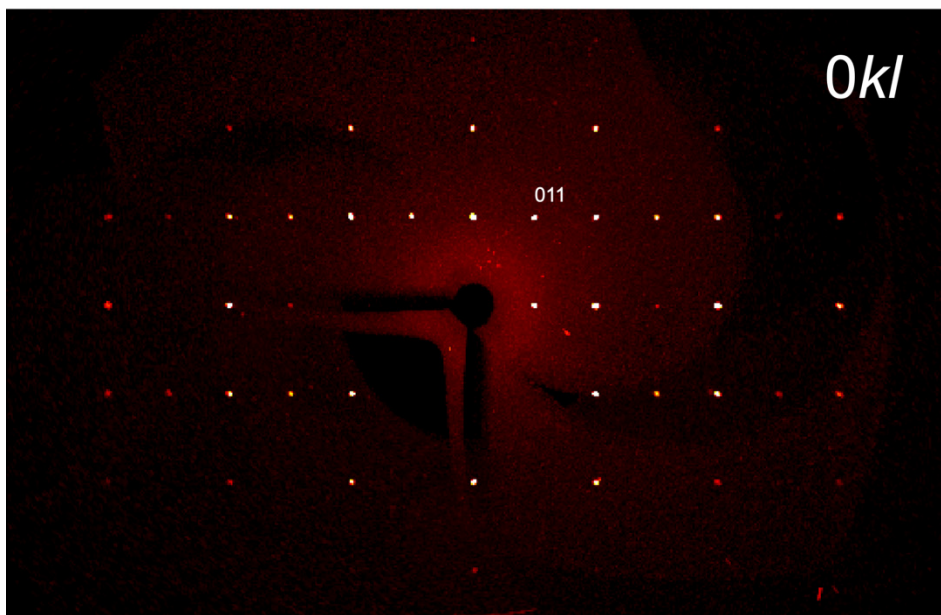
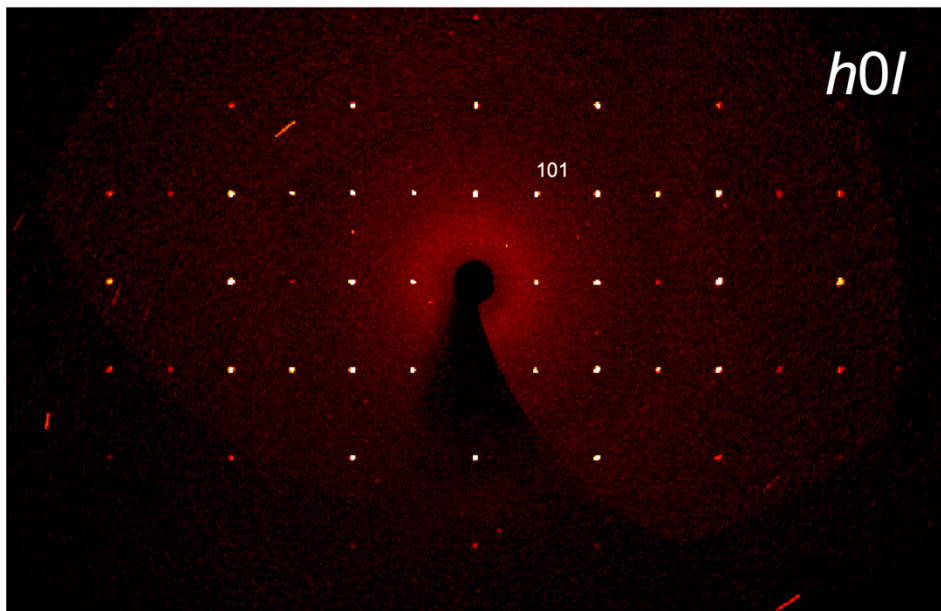
**Figure S2.** Statistically possible coordination environments of B: a) all possible distances between a given B atom and nearby Co atoms, where a red “X” means the Co is either too close or too far away for a bonding interaction to occur, while Co atoms marked with a green “check” are in a reasonable range; b), c) and d) show three possibilities for coordination, i.e., different combinations of the two possible Co-B bonds pointing to the left and four of the eight possible Co-B bonds pointing to the right.

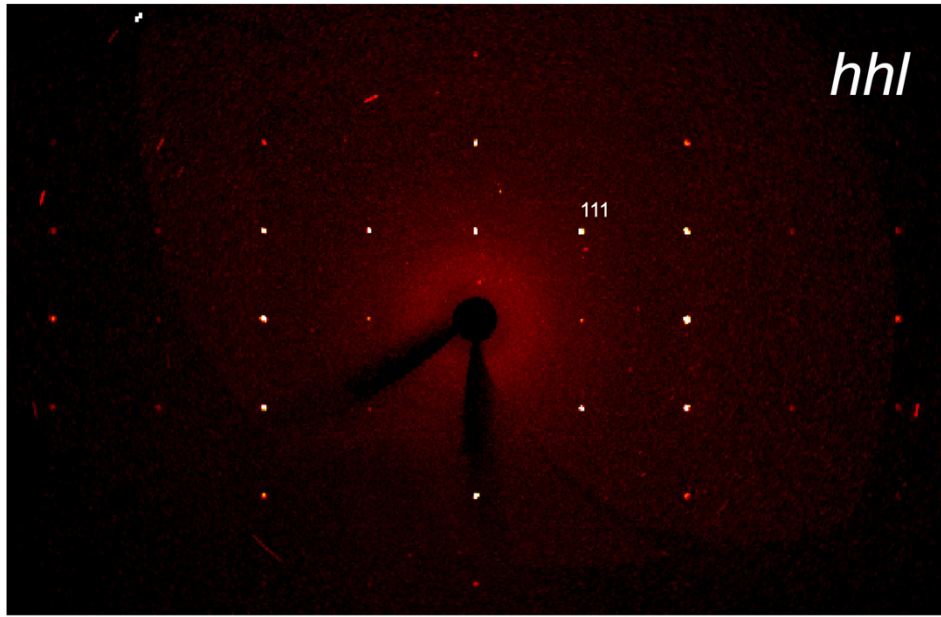


**Figure S3.** Statistically possible coordination environments of Co1 and Co2 atoms; a) and d) show all possible interatomic distances between Co1 and nearby B atoms and Co2 and nearby B atoms, respectively, where a red “X” means the atom is either too close or too far away for a bonding interaction to occur, while B atoms with a green “check” are in a reasonable range; b) and e) show possibilities for coordination of Co1 and Co2, respectively, and c) and f) show the same units rotated by 90° about the *c*-axis.

### **Supplemental discussion to Figures S2 and S3 regarding Co–B interatomic environment.**

In the CeCo<sub>3</sub>B<sub>2</sub>-like ordered structure of MgCo<sub>3</sub>B<sub>2</sub>, Co is coordinated to four B atoms (at a distance of 2.035 Å), four Co atoms within the Kagomé layer (2.446 Å), and four Mg atoms (2.852 Å). Geometrically, this places 12-coordinate Co at the center of a Mg<sub>4</sub>B<sub>4</sub> rhombic prism, the vertical faces of which are capped with Co atoms (Figure 4e). In the disordered structure, split Co and B sites distort the geometry of this polyhedron and bring about a myriad of possible polyhedra depending on the specific Co and B sites occupied in a given unit cell. Ignoring the Co–Co and Co–Mg interactions, one is left with a CoB<sub>4</sub> unit that is nearly square planar in the average (CeCo<sub>3</sub>B<sub>2</sub>-like) structure with bond angles of 87.9° and 92.1°, while B sits in the center of trigonal prisms to form BC<sub>6</sub> units (Figure 4d). In the disordered structure, when all split sites are taken into consideration, the lengths of possible Co–B separations range from 1.456 Å to 2.481 Å. Both of these extremes are unrealistic for a Co–B bonding interaction. We impose a lower cutoff of 1.95 Å and an upper bound of 2.30 Å to define a “reasonable” Co–B interaction, based on analysis of reported Co–B distances in the ICSD.<sup>2</sup> Figure S2a shows all possible B–Co distances for a given B atom. With the bond cutoffs from above, the two shortest (1.456 and 1.735 Å) and the longest (2.481 Å) distances can be eliminated, leaving two possible distances of 2.034 and 2.242 Å. Figure S2b-d displays three statistical possibilities for the BC<sub>6</sub> units composed of combinations of these two “allowed” bonding interactions. Figures S3a and S3d show all possible Co–B distances for Co1 in 3g site and for Co2 in a 6*i* site, respectively. While the geometry of the CoB<sub>4</sub> unit centered on Co2 may appear to be tending toward tetrahedral (Figure S3e), rotation by 90° reveals that the atoms are still close to the plane of what was originally a square planar moiety (Figure S3f). Note that not every statistically possible combination of reasonable bonding interactions is plotted in Figures S2 and S3.





**Figures S4.** Precession images of reconstructed reciprocal planes  $h0l$ ,  $0kl$ , and  $hh\bar{l}$ , showing no indications of superstructure reflections, satellite reflections, or diffuse scattering.

## MgNi<sub>3</sub>B<sub>2</sub>-type structure, *P*6<sub>4</sub>22

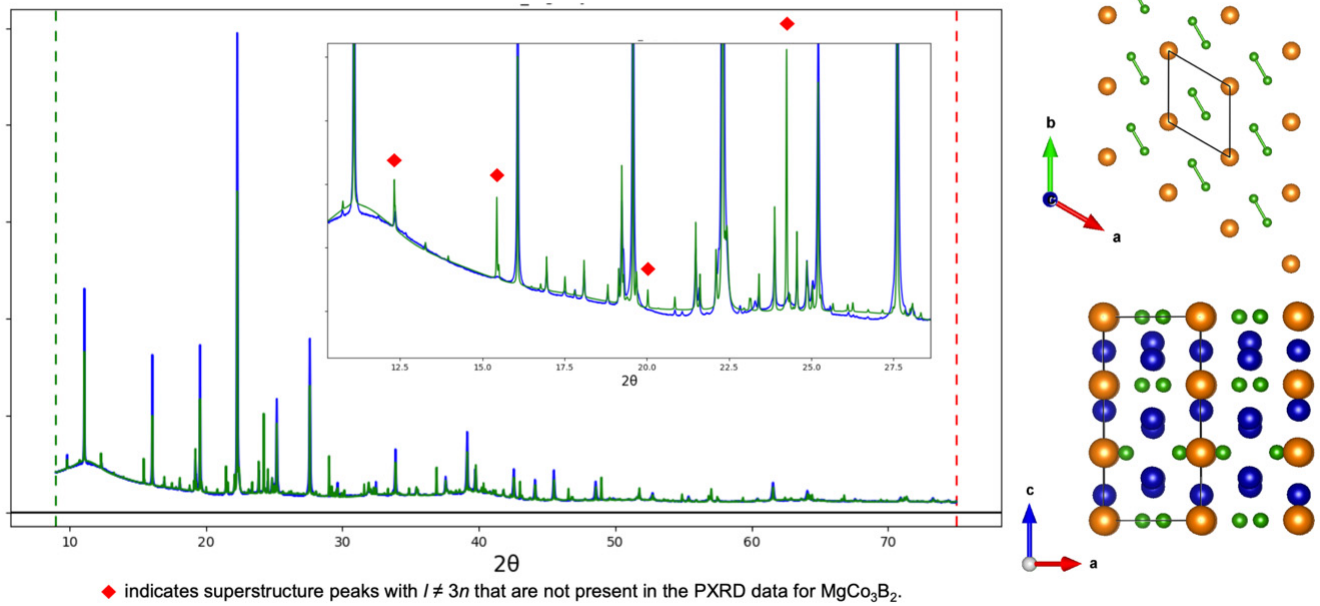


**Figure S5.** Rietveld refinement of high-resolution PXRD data for MgCo<sub>3</sub>B<sub>2</sub> using a structural model in the MgNi<sub>3</sub>B<sub>2</sub> structure type, with colored diamonds indicating diffraction peaks whose calculated and observed intensities deviate significantly; blue trace – experimental PXRD data, green trace is the calculated profile. Scale factor, 36 background coefficients, unit cell parameters for MgCo<sub>3</sub>B<sub>2</sub>, and phase fractions are refined for each pattern.

Sample absorption ( $\mu \cdot r$ ) and unit cell parameters for known impurity phases were initially refined and then fixed for consistency across all refinements shown in Figures S5-S7.

### ZrCo<sub>3</sub>B<sub>2</sub>-type structure, $R\bar{3}$

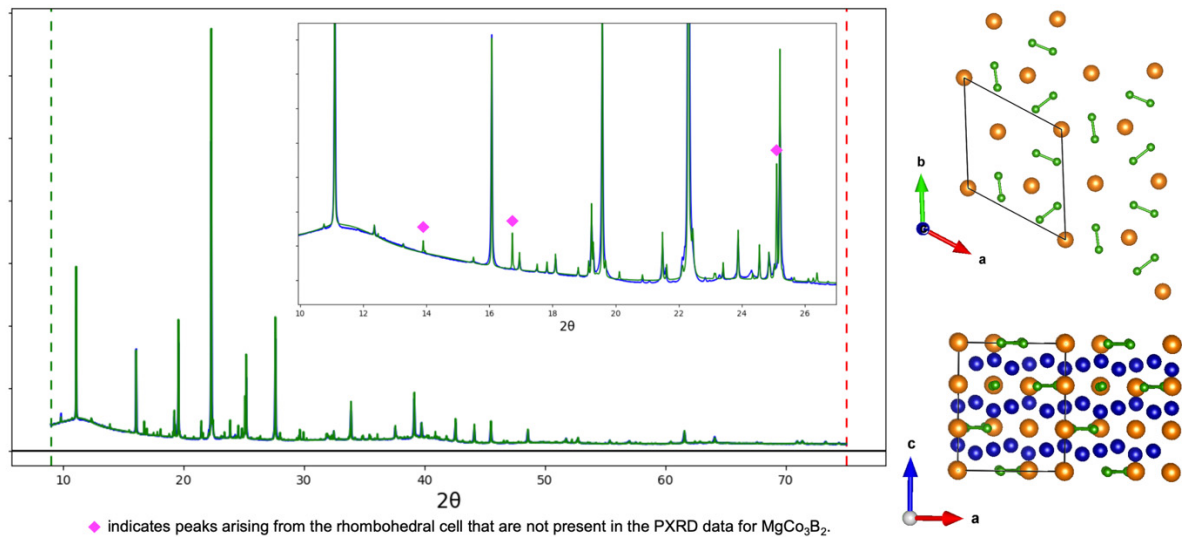
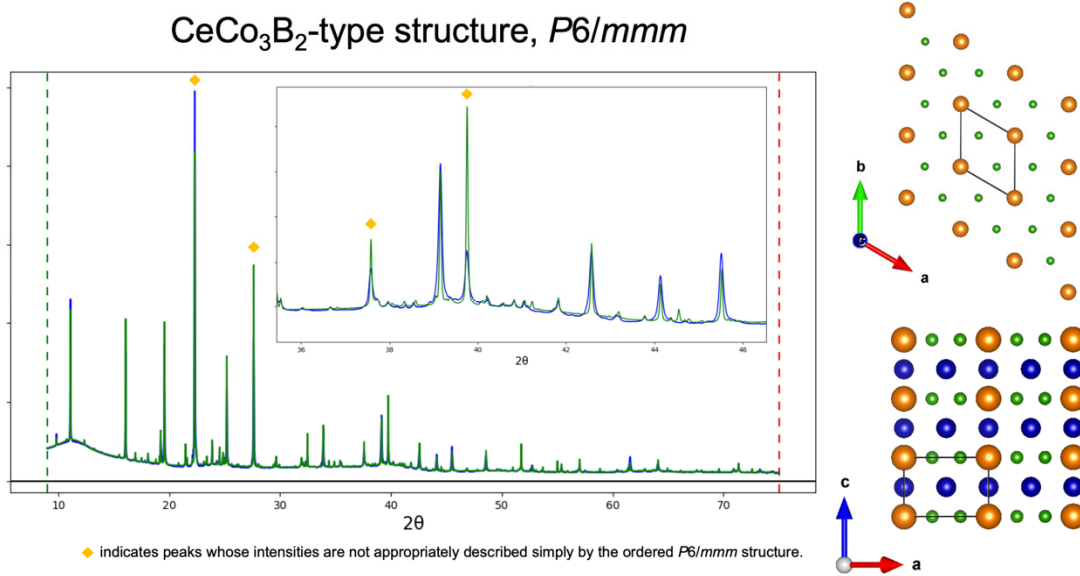


**Figure S6.** Rietveld refinement of high-resolution PXRD data for MgCo<sub>3</sub>B<sub>2</sub> using a structural model in the ZrCo<sub>3</sub>B<sub>2</sub> structure type, with colored diamonds indicating diffraction peaks whose calculated and observed intensities deviate significantly; blue trace – experimental PXRD data, green trace is the calculated profile. Scale factor, 36 background coefficients, unit cell parameters for MgCo<sub>3</sub>B<sub>2</sub>, and phase fractions are refined for each pattern.

Sample absorption ( $\mu \cdot r$ ) and unit cell parameters for known impurity phases were initially refined and then fixed for consistency across all refinements shown in Figures S5-S7.



**Figures S7.** Rietveld refinement of high-resolution PXRD data for MgCo<sub>3</sub>B<sub>2</sub> using a structural model in the CeCo<sub>3</sub>B<sub>2</sub> structure type, with colored diamonds indicating diffraction peaks whose calculated and observed intensities deviate significantly; blue trace – experimental PXRD data, green trace is the calculated profile. Scale factor, 36 background coefficients, unit cell parameters for MgCo<sub>3</sub>B<sub>2</sub>, and phase fractions are refined for each pattern.

Sample absorption ( $\mu \cdot r$ ) and unit cell parameters for known impurity phases were initially refined and then fixed for consistency across all refinements shown in Figures S5-S7.

**Table S5.** Comparison of refinement parameters from Rietveld refinements of four structural models of MgCo<sub>3</sub>B<sub>2</sub>: MgNi<sub>3</sub>B<sub>2</sub>, ZrCo<sub>3</sub>B<sub>2</sub>, CeCo<sub>3</sub>B<sub>2</sub>, and the disordered model obtained from solving structure using SCXRD data. Note that the statistics shown for the SCXRD model differ from the final parameters listed in Table S6 below since sample parameters have not yet been refined.

Model	wR	GoF
MgNi <sub>3</sub> B <sub>2</sub>	19.747	81.12
ZrCo <sub>3</sub> B <sub>2</sub>	13.098	53.81
CeCo <sub>3</sub> B <sub>2</sub>	15.144	62.21
MgCo <sub>3</sub> B <sub>2</sub> (model from SCXRD)	11.759	48.30

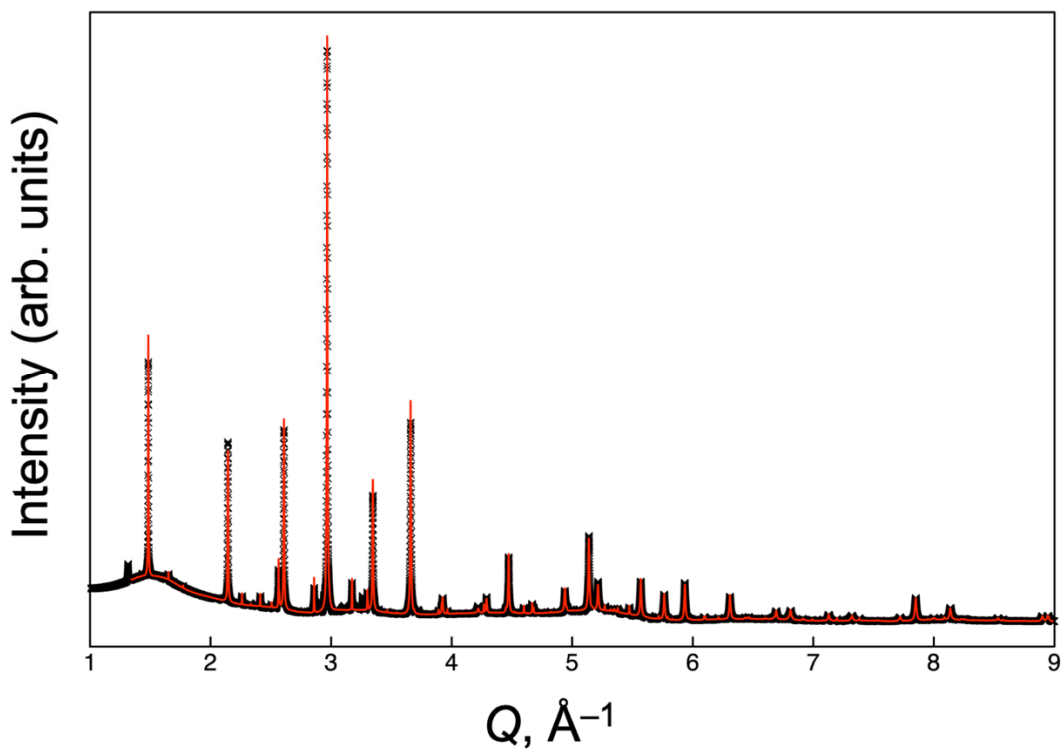


**Figure S8.** High-resolution PXRD of  $\text{MgCo}_3\text{B}_2$  (BXDS, Canadian Light Source,  $\lambda = 0.81931 \text{\AA}$ ). Black crosses are the observed data points and the red line is the fit calculated from Rietveld refinement, including impurity phases. Scale factor, background coefficients (36 Chebyshev), phase fractions, unit cell parameters, absorption ( $\mu \cdot r$ ), sample displacement relative to the beam, domain size, and microstrain were refined.

**Table S6.** Unit cell, refinement statistics, and sample parameters for MgCo<sub>3</sub>B<sub>2</sub> from Rietveld refinement of HR-PXRD (BXDS, CLS,  $\lambda = 0.81931 \text{ \AA}$ ) using the disordered model solved from SCXRD. Excluded regions include peaks (relative intensity <5%) that cannot be matched to a known phase composed of Mg, Co, B, C, and/or H; the  $q$ -ranges indicated were marked to be eliminated from the Rietveld refinement. The dimensionless value for sample absorption in Debye-Scherrer geometry,  $\mu \cdot r$ , was refined because the relatively low X-ray energy (15.133 keV) together with heavy atoms (Co) resulted in moderate to strong sample absorption, indicated by the refined ( $\mu \cdot r$ ) value of 1.779. Sample displacement parallel and perpendicular to the beam, domain size and microstrain to account for slight observed peak broadening were also refined. Additionally, the powder sample on which HR-PXRD data were acquired includes four identified impurity phases: Mg, MgO, MgCo<sub>3</sub>C, and Co<sub>2</sub>B, with MgCo<sub>3</sub>B<sub>2</sub> as the major phase (~ 90 wt. %). MgCo<sub>3</sub>C (1.71(2) wt. %) is a ternary carbide that adopts a cubic antiperovskite structure,<sup>8</sup> though it is unclear at the moment whether B is also present in this phase, i.e. MgCo<sub>3</sub>(B,C). Structure models were taken from ICSD database:<sup>2</sup> Mg [PDF-01-080-4430], MgO [PDF-01-090-2418], MgCo<sub>3</sub>C [PDF-01-089-7236], Co<sub>2</sub>B [PDF-01-090-5420].

Empirical formula	MgCo <sub>3</sub> B <sub>2</sub>
Space group, $Z$	$P6/mmm$ (#191), 1
Cell parameters: $a$ , Å	4.89245(2)
$c$ , Å	2.93110(1)
$V$ , Å <sup>3</sup>	60.7594(3)
Cell wt., amu	222.72
Crystal density, g cm <sup>-3</sup>	6.0918
Temperature, K	293
Wavelength, Å (keV)	0.81931 (15.133)
Capillary inner radius, mm	0.25
Refined $\mu \cdot r$	1.7790
Range of $\theta$ , °	10.0–75.0
Number of datapoints	25099
Number of parameters refined	48
$wR$	0.03790
GoF	15.71
Refined sample displacement $x \perp$ beam	-45.3756
Refined sample displacement $y \parallel$ beam	102.8148
Domain size (isotropic equatorial), μm	0.43174
Microstrain (isotropic equatorial)	3111.1
Excluded regions, Å <sup>-1</sup>	$q < 1.336$ $1.418 < q < 1.456$

	2.743 < $q$ < 2.821
	3.022 < $q$ < 3.123
	3.201 < $q$ < 3.280
Phase fractions of identified phases and their weight %	
	MgCo <sub>3</sub> B <sub>2</sub> 89.15(9) wt. %
	Mg                  4.32(4) wt. %
	MgO                3.43(8) wt. %
	MgCo <sub>3</sub> C       1.71(2) wt %
	Co <sub>2</sub> B            1.39(2) wt. %

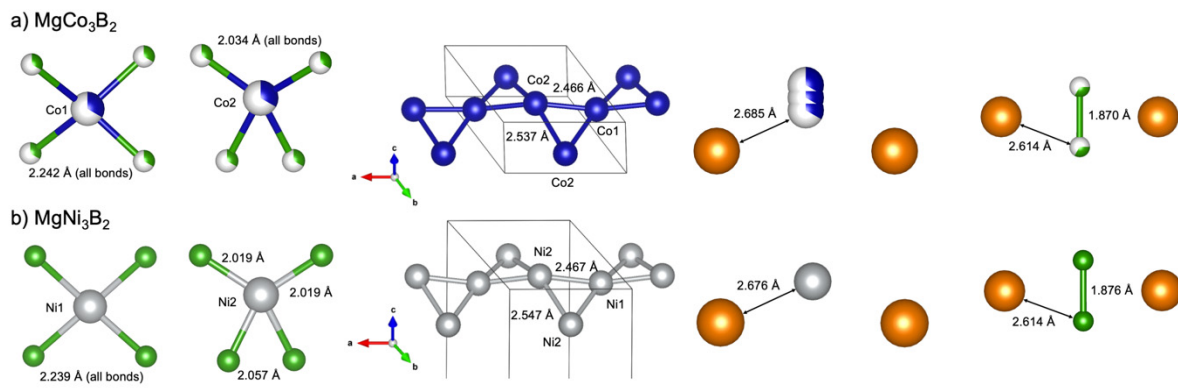


**Figure S9.** Comparison of equivalent interatomic distances between disordered  $\text{MgCo}_3\text{B}_2$  and chiral  $\text{MgNi}_3\text{B}_2$  structures [PDF-01-075-8152].

**Table S7.** Bader charge analysis on MgNi<sub>3</sub>B<sub>2</sub>, ZrCo<sub>3</sub>B<sub>2</sub>, and MgCo<sub>3</sub>B<sub>2</sub> in the MgNi<sub>3</sub>B<sub>2</sub> and ZrCo<sub>3</sub>B<sub>2</sub> structure types. Positive (negative) numbers indicate electron gain (loss).

Phase	Average charge transfer based on Bader analysis		
	Mg/Zr	Co/Ni	B
MgNi <sub>3</sub> B <sub>2</sub>	-1.5418	0.2730	0.3614
ZrCo <sub>3</sub> B <sub>2</sub>	-1.5263	0.2210	0.4317
MgCo <sub>3</sub> B <sub>2</sub> (MgNi <sub>3</sub> B <sub>2</sub> -type)	-1.5506	0.2540	0.3943
MgCo <sub>3</sub> B <sub>2</sub> (ZrCo <sub>3</sub> B <sub>2</sub> -type)	-1.5531	0.2508	0.4003

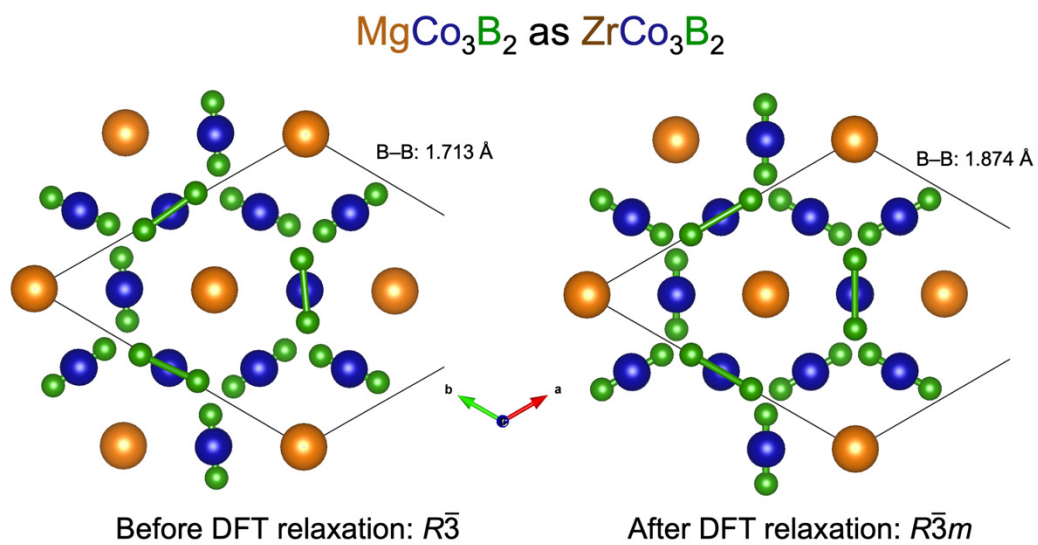


**Figure S10.** Models of MgCo<sub>3</sub>B<sub>2</sub> in the ZrCo<sub>3</sub>B<sub>2</sub> structure type showing changes in symmetry and B–B bond length before and after DFT relaxation.

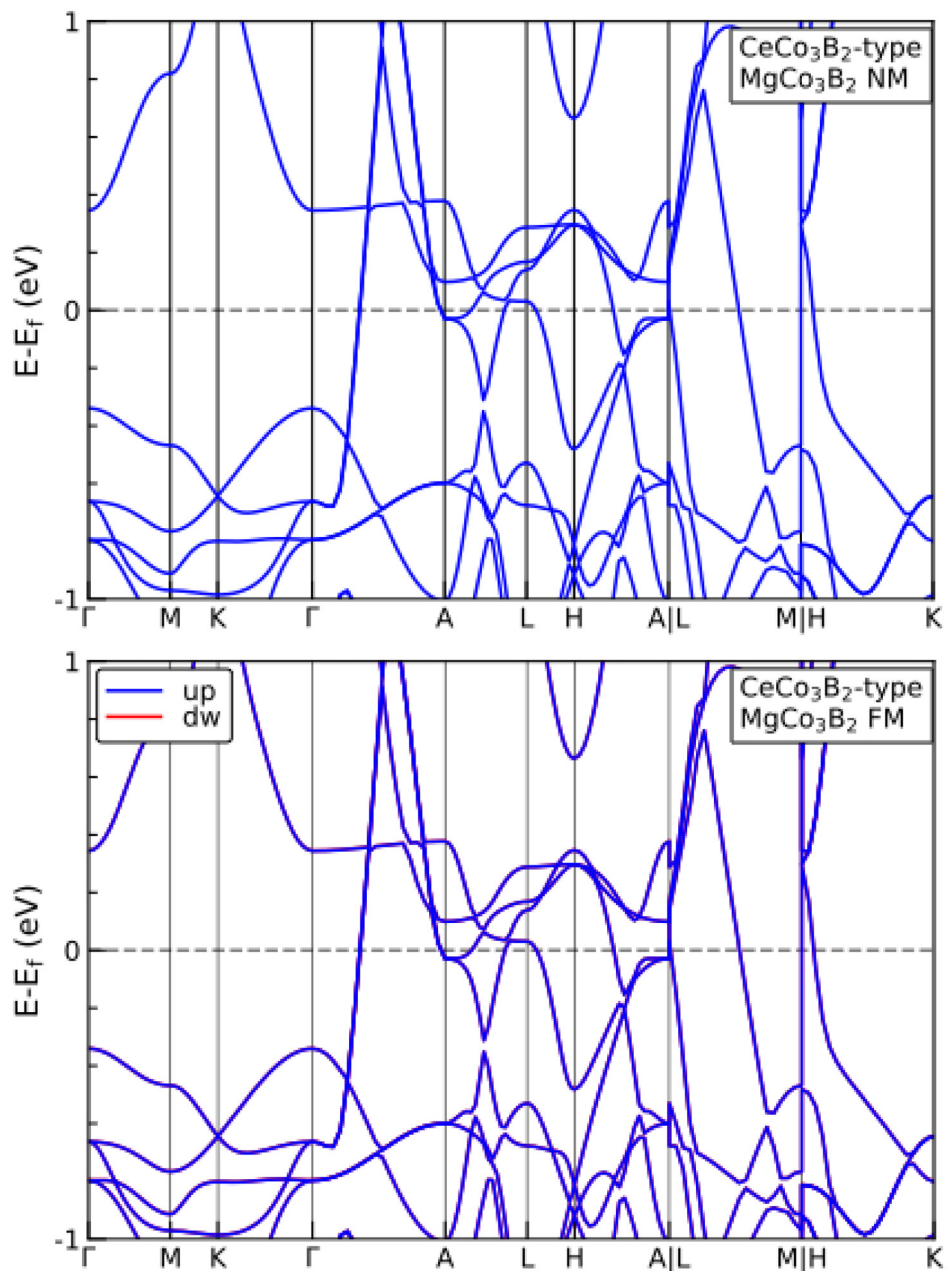


**Figure S11.** Non-spin-polarized (top) and spin-polarized (bottom) band structures for  $\text{MgCo}_3\text{B}_2$  in the  $\text{CeCo}_3\text{B}_2$  structure type showing no splitting of spin-up and spin-down bands into different energy levels.

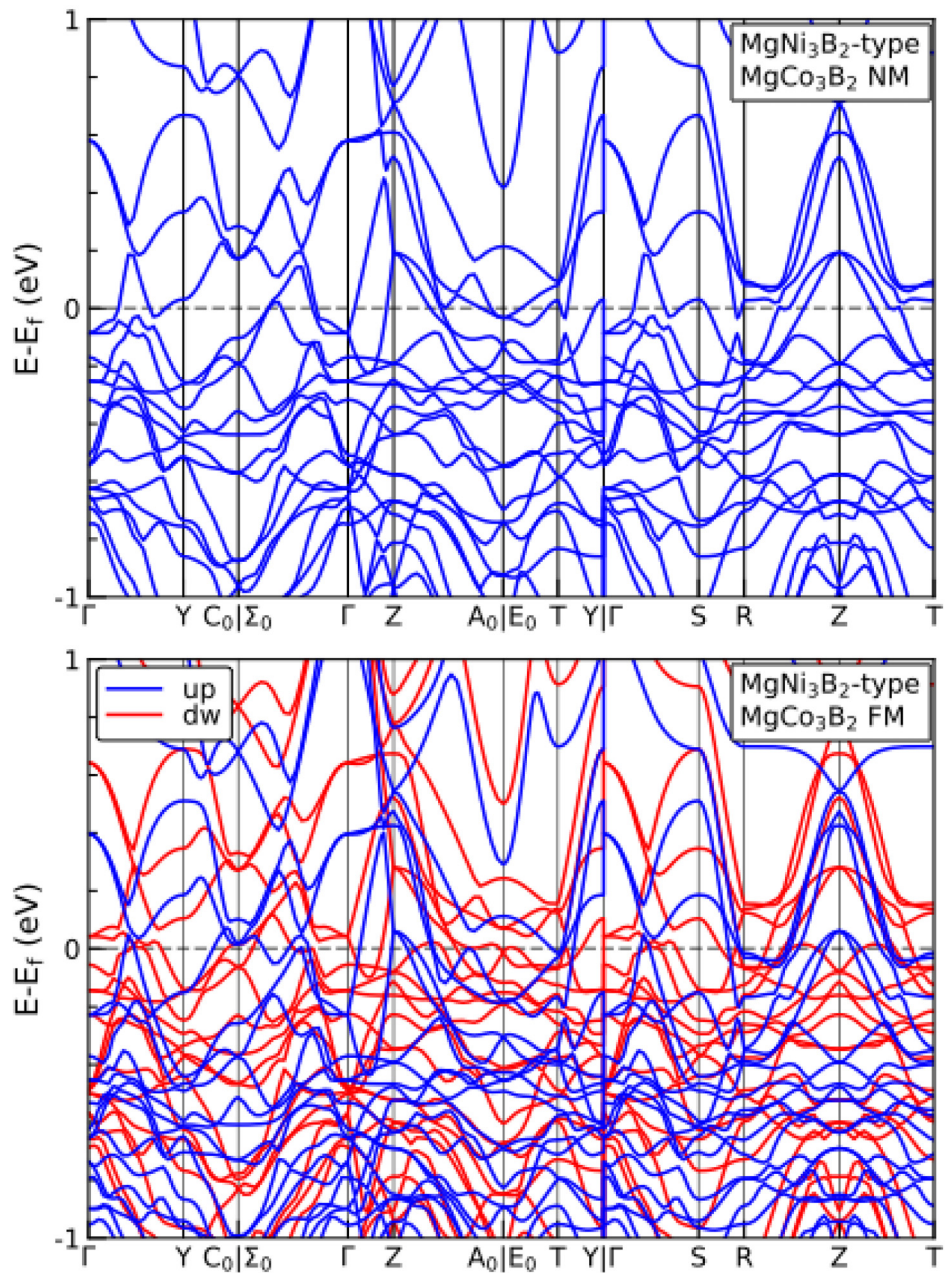


**Figure S12.** Non-spin-polarized band structures for  $\text{MgCo}_3\text{B}_2$  in the  $\text{MgNi}_3\text{B}_2$  structure type (top) and spin-polarized band structure for the ferromagnetic excited state (see Table 2) of  $\text{MgCo}_3\text{B}_2$  in the  $\text{MgNi}_3\text{B}_2$  structure type (bottom) showing spin-up and spin-down bands split into different energy levels.

**Table S8.** Unit cell parameters for MgCo<sub>3</sub>B<sub>2</sub> from 500 K to 1169 K from sequential Rietveld refinement of PXRD of a pre-reacted sample sealed in a silica capillary under vacuum (Figure 5a).

Frame	T, K	a, Å	c, Å	V, Å <sup>3</sup>
2	500	4.9033(2)	2.9370(1)	61.153(3)
3	520	4.9061(1)	2.9385(1)	61.253(3)
4	538	4.9062(1)	2.9384(1)	61.254(3)
5	557	4.9080(1)	2.9394(1)	61.319(3)
6	575	4.9089(1)	2.9399(1)	61.353(3)
7	594	4.9104(1)	2.9407(1)	61.406(3)
8	613	4.9121(1)	2.9415(1)	61.468(3)
9	631	4.9127(1)	2.9419(1)	61.490(3)
10	650	4.9145(1)	2.9428(1)	61.553(3)
11	669	4.9158(1)	2.9435(1)	61.601(3)
12	688	4.9172(1)	2.9441(1)	61.648(3)
13	708	4.9185(1)	2.9448(1)	61.696(3)
14	727	4.9202(1)	2.9458(1)	61.759(3)
15	746	4.9220(1)	2.9466(1)	61.821(3)
16	766	4.9228(1)	2.9470(1)	61.851(3)
17	786	4.9243(1)	2.9478(1)	61.905(3)
18	805	4.9264(1)	2.9489(1)	61.981(3)
19	827	4.9274(1)	2.9494(1)	62.015(3)
20	846	4.9297(2)	2.9506(1)	62.099(3)
21	866	4.9304(2)	2.9510(1)	62.126(3)
22	888	4.9323(2)	2.9519(1)	62.192(3)
23	908	4.9342(2)	2.9529(1)	62.259(3)
24	930	4.9359(2)	2.9536(1)	62.319(3)
25	952	4.9371(2)	2.9543(1)	62.362(3)
26	971	4.9387(2)	2.9551(1)	62.419(3)
27	992	4.9405(2)	2.9559(2)	62.484(3)
28	1014	4.9422(2)	2.9566(2)	62.542(4)
29	1038	4.9435(2)	2.9570(2)	62.582(4)
30	1058	4.9453(2)	2.9577(2)	62.644(5)
31	1083	4.9471(3)	2.9581(2)	62.698(5)
32	1102	4.9489(3)	2.9587(3)	62.754(6)
33	1126	4.9506(3)	2.9591(3)	62.807(6)
34	1152	4.9527(4)	2.9597(3)	62.874(7)
35	1168	4.9546(4)	2.9602(3)	62.931(8)
36	1169	4.9546(4)	2.9603(4)	62.934(8)
37	1146	4.9525(5)	2.9594(4)	62.861(9)

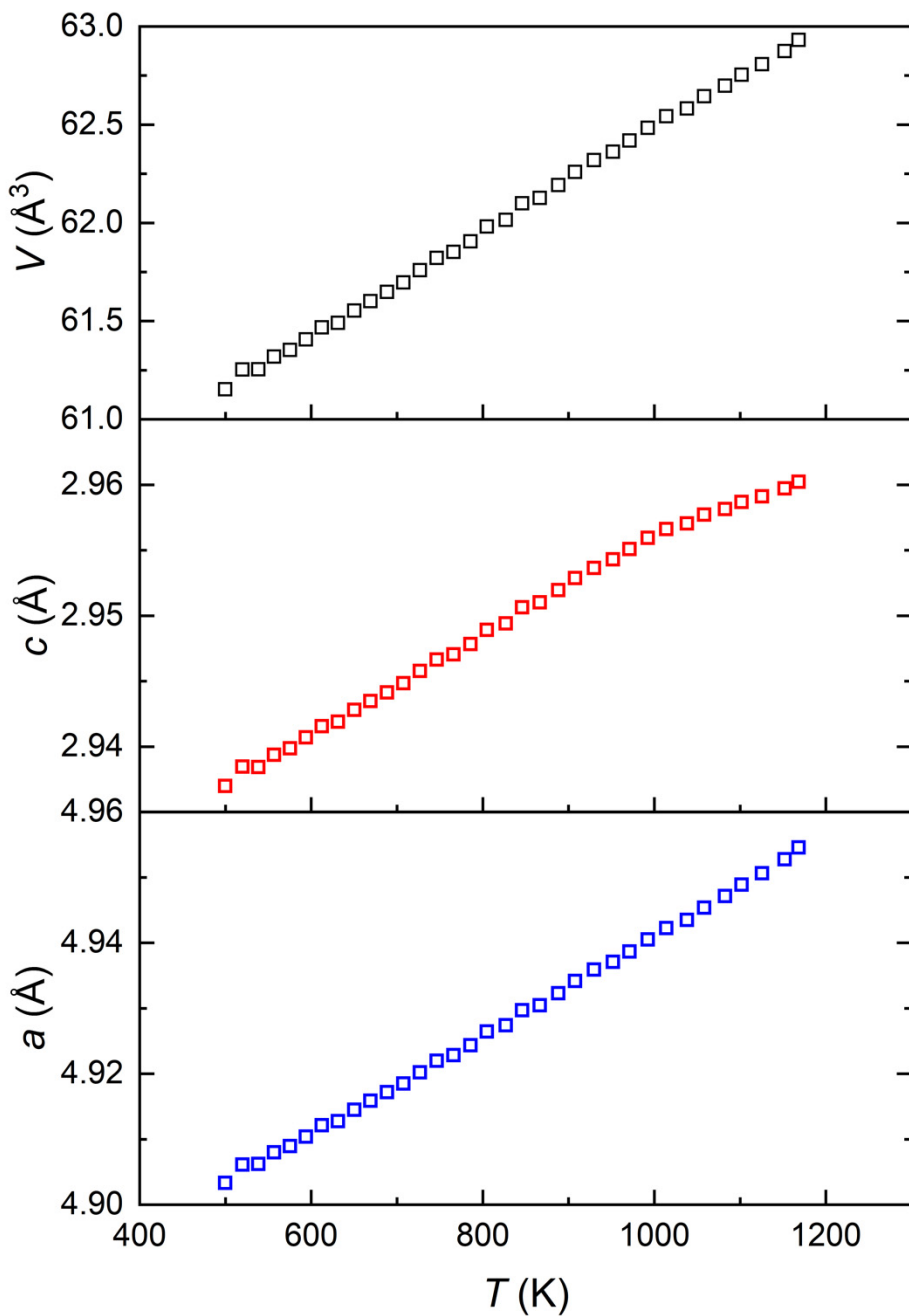


**Figure S13.** Temperature-dependence of unit cell volume and unit cell parameters. Linear fits of the data in the range 500 to 1000 K give the following values for coefficient of thermal expansion:  $1.52(1) \times 10^{-5} \text{ K}^{-1}$  for  $a$ ,  $1.301(9) \times 10^{-5} \text{ K}^{-1}$  for  $c$ , and  $4.39(3) \times 10^{-5} \text{ K}^{-1}$  for  $V$ .

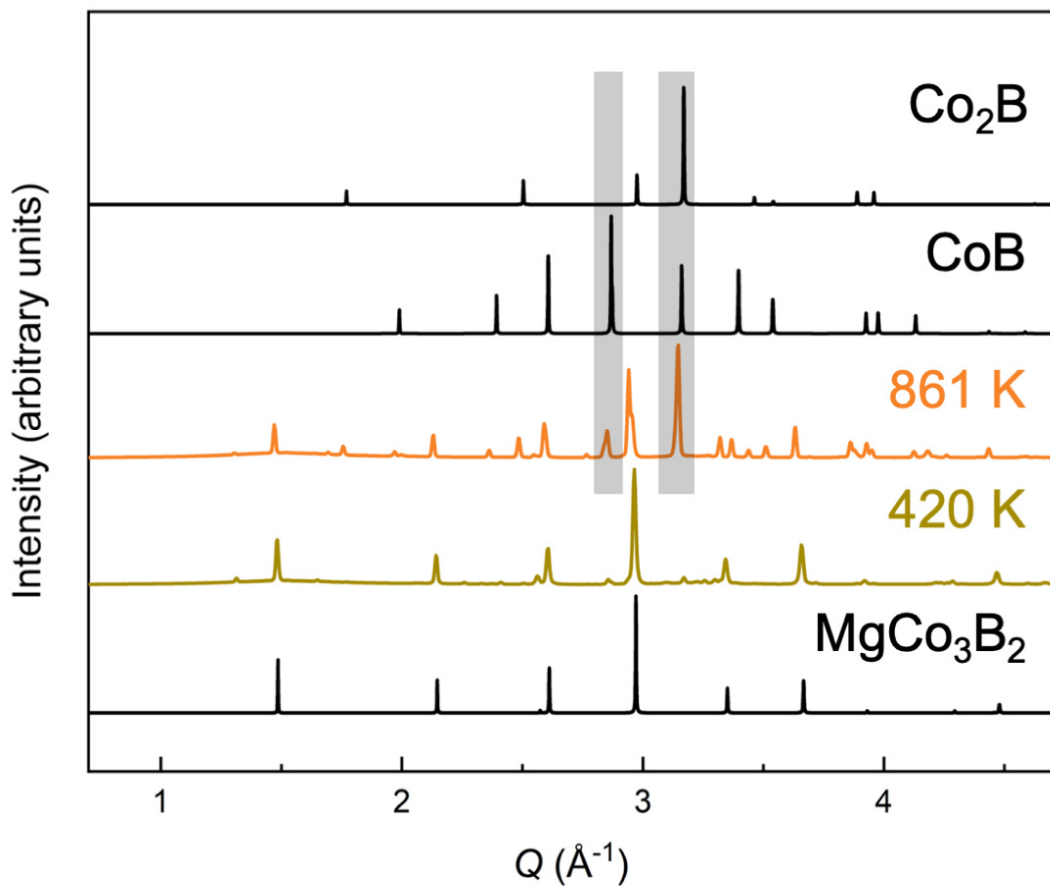


**Figure S14.** Comparison of initial and final PXRD patterns from temperature-resolved PXRD of pre-reacted  $\text{MgCo}_3\text{B}_2$ ; see Figure 5 for the complete waterfall diagram. The PXRD pattern in yellow is obtained at 420 K upon heating; the PXRD pattern in orange is obtained at 861 K upon cooling, e.g. after heat treatment up to 1169 K. Gray boxes highlight major peaks for decomposition products  $\text{Co}_2\text{B}$  and  $\text{CoB}$  that are present after heating above 992 K but minimally present in the starting sample at  $\sim 420$  K. Measurements were made at beamline 28-ID-2 NSLS-II BNL at wavelength  $\lambda = 0.1824 \text{\AA}$ .

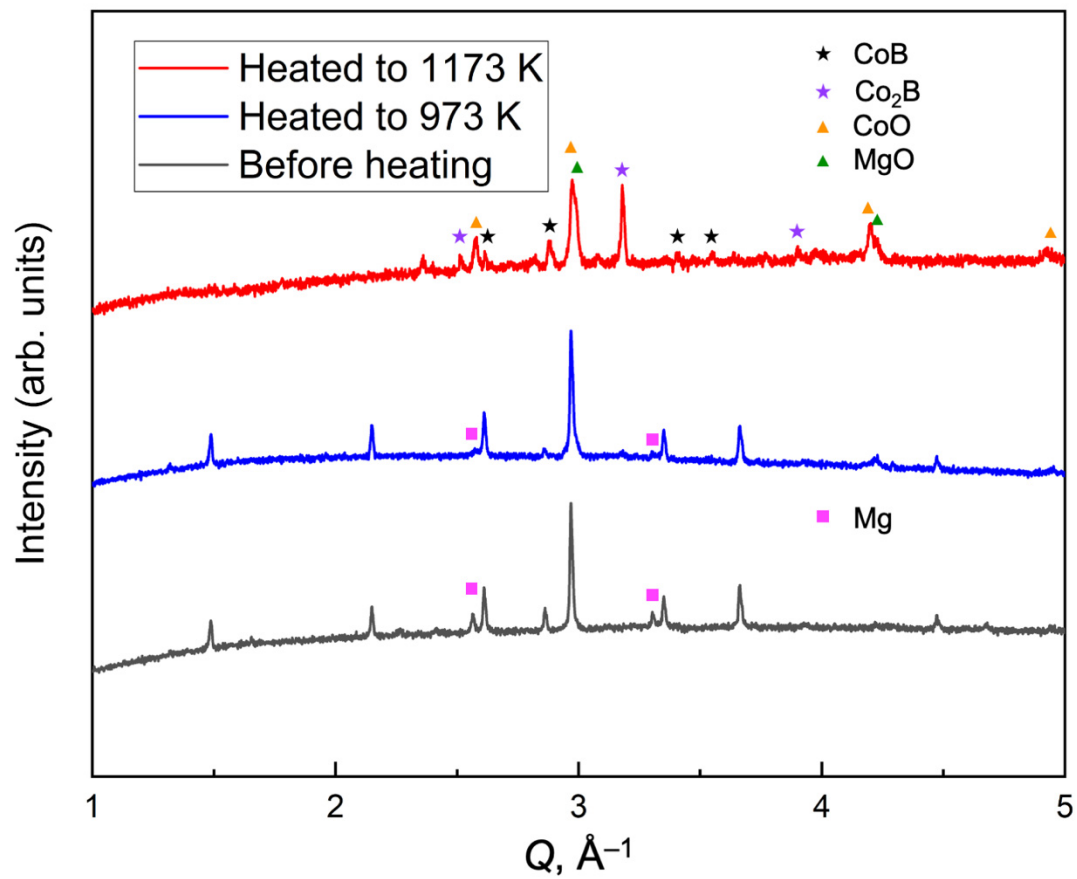


**Figure S15.** Comparison of PXRD patterns of  $\text{MgCo}_3\text{B}_2$  sample in air at room temperature (bottom, black) after heating a sample to 973 K in air (middle, blue), and after heating to 1173 K in air (top, red).

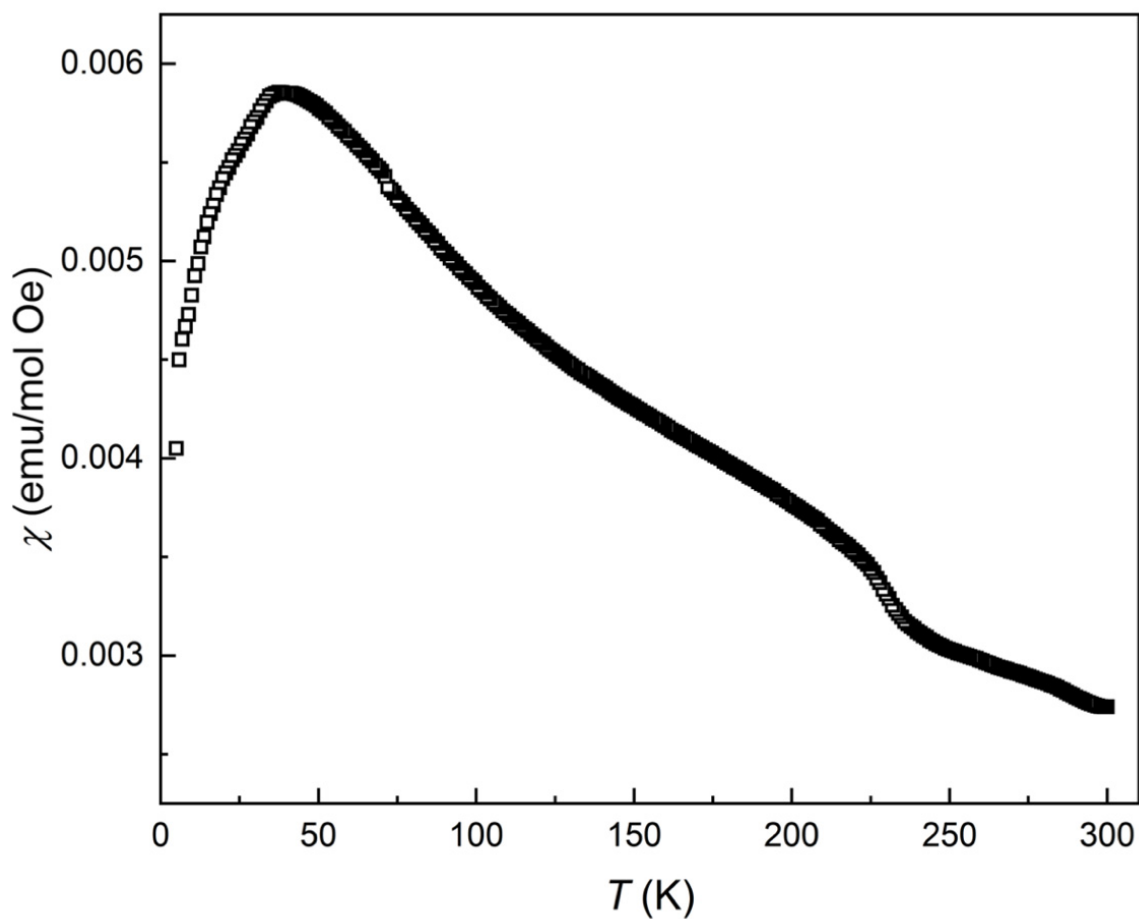


**Figure S16.** Magnetic susceptibility of  $\text{MgCo}_3\text{B}_2$  as a function of temperature at 1 kOe. The steep decline in magnetization observed below  $\sim 36$  K is attributed to the superconducting transition of a minor impurity of  $\text{MgB}_2$  ( $T_c = 39$  K)<sup>9</sup> not observed in HR-PXRD data.

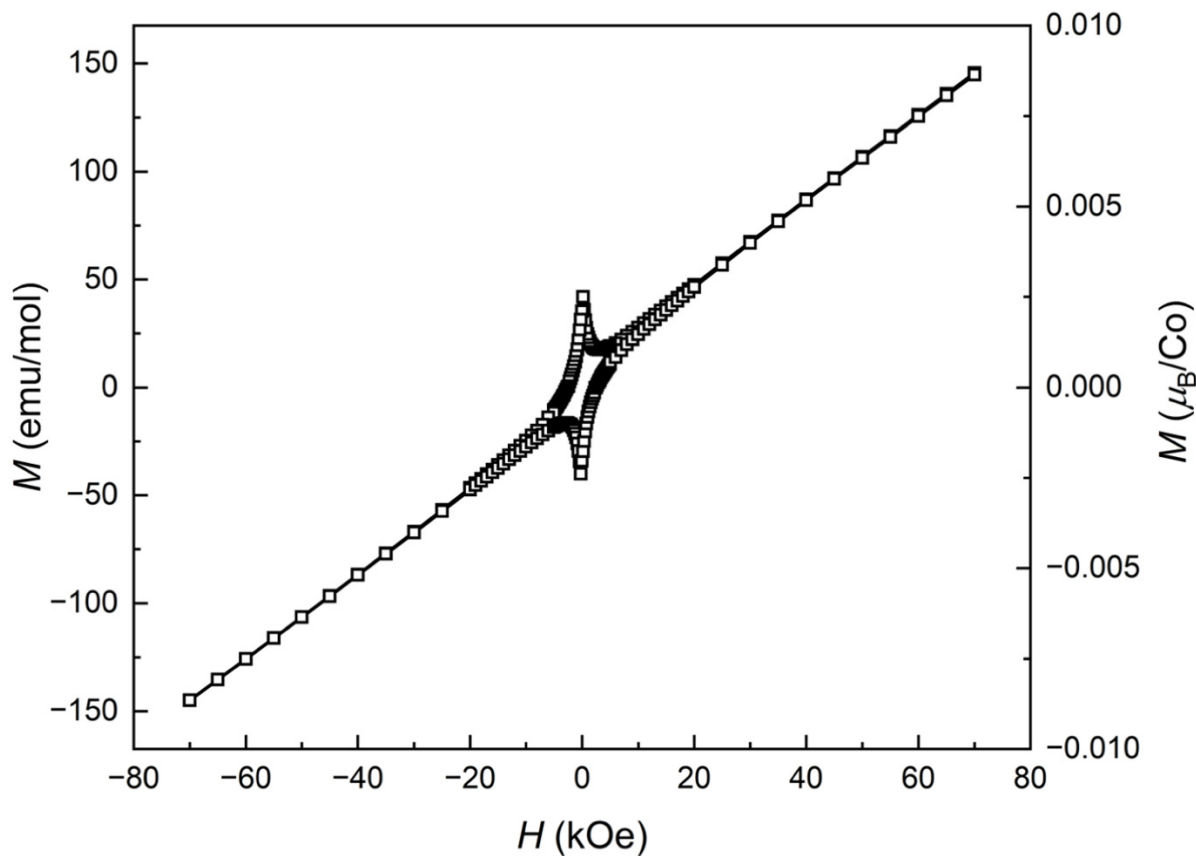


**Figure S17.** Isothermal magnetization of  $\text{MgCo}_3\text{B}_2$  as a function of field at 5 K. Superconducting hysteresis at low field is apparent from the peak in magnetization around  $H = 0$  kOe. To estimate an upper bound on the fraction of the  $\text{MgB}_2$  impurity phase, we compared the peak magnetization at 0 kOe (0.188 emu/g) with the reported magnetization of a sintered sample of polycrystalline  $\text{MgB}_2$ , peaking at around 450 emu/cm<sup>3</sup> at zero field for a 6 K measurement.<sup>10</sup> Assuming a pellet of 100% crystallographic density, this converts to 171 emu/g. Therefore, the  $\text{MgB}_2$  impurity fraction is estimated as  $0.188/171 \approx 0.1$  wt. %, which is unlikely to be detected by laboratory PXRD, especially considering the high background due to the fluorescence of Co under  $\text{Cu}-K\alpha$  radiation in laboratory PXRD data.

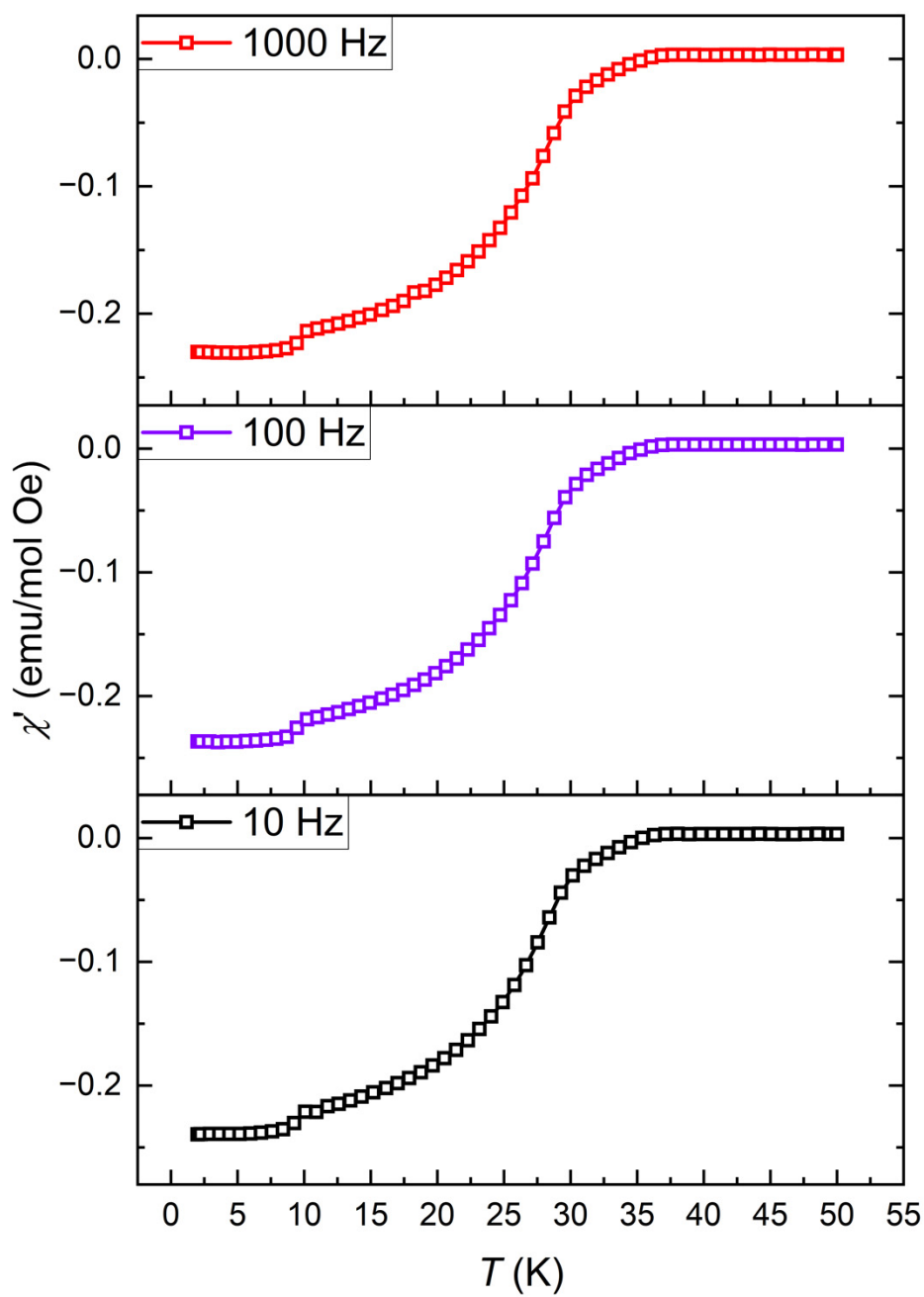


**Figure S18.** Real component of  $ac$  susceptibility of  $MgCo_3B_2$  between 2 K and 50 K at 1000 Oe  $dc$  bias field, 1 Oe  $ac$  field, and frequencies of 10, 100, and 1000 Hz.

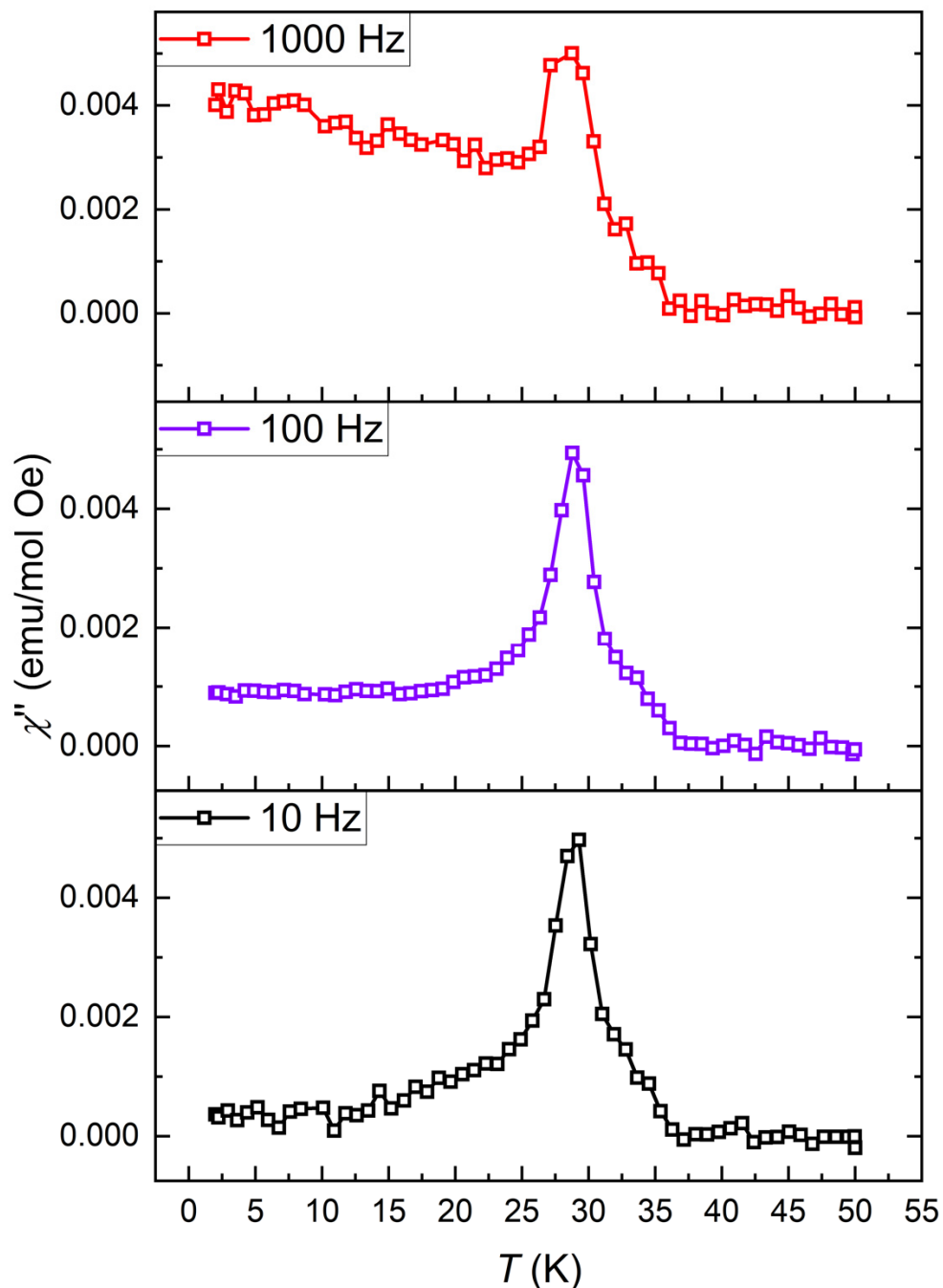


**Figure S19.** Imaginary component of *ac* susceptibility of  $\text{MgCo}_3\text{B}_2$  between 2 K and 50 K at 1000 Oe *dc* bias field, 1 Oe *ac* field, and frequencies of 10, 100, and 1000 Hz.

- (1) Toby, B. H.; Von Dreele, R. B. GSAS-II: The Genesis of a Modern Open-Source All Purpose Crystallography Software Package. *J Appl Crystallogr* **2013**, *46* (2), 544–549. <https://doi.org/10.1107/S0021889813003531>.
- (2) Zagorac, D.; Muller, H.; Ruehl, S.; Zagorac, J.; Rehme, S. Recent Developments in the Inorganic Crystal Structure Database: Theoretical Crystal Structure Data and Related Features. *J Appl Crystallogr* **2019**, *52*, 918–925. <https://doi.org/10.1107/S160057671900997X>.
- (3) Villars, P.; Cenzual, K. Pearson's Crystal Data – Crystal Structure Database for Inorganic Compounds. ASM International: Materials Park, OH, USA 2016.
- (4) Kuz'ma, Yu. B.; Kripyakevich, P. I.; Bilonizhko, N. S. Crystal Structure of CeCo<sub>3</sub>B<sub>2</sub> and Analogous Compounds. *Dopovidi Akademii Nauk Ukrains'koi RSR, Seriya A: Fizyko-Tekhnichni ta Matematichni Nauki* **1969**, *31* (10), 939–941.
- (5) Ku, H. C.; Meissner, G. P. Crystal Structure and Physical Properties of New Ternary Rare Earth Borides. *Journal of the Less-Common Metals* **1981**, *78*, 99–107.
- (6) Manfrinetti, P.; Pani, M.; Dhar, S. K.; Kulkarni, R. Structure, Transport and Magnetic Properties of MgNi<sub>3</sub>B<sub>2</sub>. *J Alloys Compd* **2007**, *428* (1–2), 94–98. <https://doi.org/10.1016/j.jallcom.2006.03.048>.
- (7) Voroshilov, Yu. V.; Kuz'ma, Yu. B. Reaction of Zirconium with the Transition Metals and Boron. *Soviet Powder Metallurgy and Metal Ceramics* **1969**, *8* (11), 941–944.
- (8) Huettert, L. J.; Stadelmaier, H. H. Ternary Carbides of Transition Metals with Aluminum and Magnesium. *Acta Metallurgica* **1958**, *6*, 367–370.
- (9) Nagamatsu, J.; Nakagawa, N.; Muranaka, T.; Zenitani, Y.; Akimitsu, J. Superconductivity at 39K in Magnesium Diboride. *Nature* **2001**, *401*, 63–64.
- (10) Finnemore, D. K.; Ostenson, J. E.; Bud'ko, S. L.; Lapertot, G.; Canfield, P. C. Thermodynamic and Transport Properties of Superconducting Mg<sub>10</sub>B<sub>2</sub>. *Phys Rev Lett* **2001**, *86* (11), 2420–2422. <https://doi.org/10.1103/PhysRevLett.86.2420>.